The University
of Manchester

Eye movement instabilities and nystagmus can be predicted by a nonlinear dynamics model of the saccadic system

Akman, O. E. and Broomhead, D. S. and Abadi, R. V. and Clement, R. A.

2005

MIMS EPrint: **2006.23**

Manchester Institute for Mathematical Sciences

School of Mathematics

The University of Manchester

Eye movement instabilities and nystagmus can be predicted by a nonlinear dynamics model of the saccadic system

O.E. Akman[*]

The School of Mathematics, The University of Manchester

P.O. Box 88, Manchester M60 1QD, U.K.

D.S. Broomhead

The School of Mathematics, The University of Manchester

P.O. Box 88, Manchester M60 1QD, U.K.

R.V. Abadi

Faculty of Life Sciences, Moffat Building, The University of Manchester

Sackville St, Manchester M60 1QD, U.K.

R.A. Clement

Visual Sciences Unit, Institute of Child Health, U.C.L.

30 Guilford Street, London WC1N 1EH, U.K.

Abstract

The study of eye movement control and oculomotor disorders has, for four decades, relied on control theoretic concepts for its theoretical foundation. This paper is an example of a complementary approach based on the theory of nonlinear dynamical systems. Recently, a nonlinear dynamics model of the saccadic system was developed, comprising a symmetric piecewise-smooth system of six first-order autonomous ordinary differential equations. A preliminary numerical investigation of the model revealed that in addition to generating normal saccades, it could also simulate inaccurate saccades, and the oscillatory instability known as congenital nystagmus (CN). By varying the parameters of the model, several types of CN oscillations were produced, including jerk, bidirectional jerk and pendular nystagmus.

The aim of this study was to investigate the bifurcations and attractors of the model, in order to obtain a classification of the simulated oculomotor behaviours. The application of standard stability analysis techniques, together with numerical work, revealed that the equations have a rich bifurcation structure. In addition to Hopf, homoclinic and saddlenode bifurcations organised by a Takens-Bogdanov point, the equations can undergo nonsmooth pitchfork bifurcations and nonsmooth gluing bifurcations. Evidence was also found for the existence of Hopf-initiated canards.

[*]Now at: Mathematics Institute, University of Warwick, Coventry CV4 7AL, UK

1

The simulated jerk CN waveforms were found to correspond to a pair of post-canard symmetry-related limit cycles, which exist in regions of parameter space where the equations are a slow-fast system. The slow and fast phases of the simulated oscillations were attributed to the geometry of the corresponding slow manifold. The simulated bidirectional jerk and pendular waveforms were attributed to a symmetry invariant limit cycle produced by the gluing of the asymmetric cycles.

In contrast to control models of the oculomotor system, the bifurcation analysis places clear restrictions on which kinds of behaviour are likely to be associated with each other in parameter space, enabling predictions to be made regarding the possible changes in the oscillation type that may be observed upon changing the model parameters. The analysis suggests that CN is one of a range of oculomotor disorders associated with a pathological saccadic braking signal, and that jerk and pendular nystagmus are the most probable oscillatory instabilities. Additionally, the transition from jerk CN to bidirectional jerk and pendular nystagmus observed experimentally when the gaze angle or attention level is changed is attributed to a gluing bifurcation. This suggests the possibility of manipulating the waveforms of subjects with jerk CN experimentally to produce waveforms with an extended foveation period, thereby improving visual resolution.

1   Introduction

Traditionally, the study of eye movement control and oculomotor disorders has been dominated by control theory [35], [42], [33], [41], [30], [21]. In the last few years, however, there has been increasing interest in the use of nonlinear dynamics techniques to model oculomotor control, and to analyse eye movement time series [3], [37], [25], [18], [7], [20]. The oculomotor control subsystem that is responsible for the generation of fast eye movements (saccades) has been the focus of much theoretical and experimental work [14], [42], [36], [18], [24]. A recent nonlinear dynamics model of the saccadic system proposed in [18] was found to be able to simulate normal saccades, abnormal saccades and normal saccades with a dynamic overshoot. In that work, numerical evidence was presented to show that a saccadic system model alone can generate both slow and fast eye movements. Indeed, the model was found to generate waveforms resembling those associated with the pathological oculomotor instability known as congenital nystagmus (CN), which is currently believed to be a disorder of one or more of the oculomotor subsystems responsible for the generation of non-saccadic eye movements [1].

This paper describes the results of a bifurcation analysis of the model, and presents a number of implications of the analysis for understanding saccadic abnormalities and the aetiology of CN. In section 2, a brief overview of the relevant biology is given. The derivation of the model equations is described in section 3, where it is also argued that the analysis of the model can effectively be reduced to that of the equations representing the dynamics of the neurons which generate the saccadic control signal. Section 4 presents the

main results of the bifurcation analysis, enabling the simulated waveforms to be organised around the corresponding bifurcation curves, and the morphology of each waveform to be interpreted in terms of the corresponding fixed point or limit cycle attractor. The results of section 4 are summarised in figure 15.

Lastly, the biological implications of the analysis are discussed in section 5. Chief amongst these is the suggestion that CN may be a disorder of the saccadic system. This view conflicts with the characterisation of CN as an abnormality of one of the oculomotor control subsystems responsible for slow eye movement control and fixation, based on the findings of many of the control models [33], [30], [21]. In these models, it is implicitly assumed that the saccadic system is functioning within its normal parameter range. By contrast, the analysis presented here implies that CN may be part of a range of disorders produced by an abnormal saccadic braking signal. Moreover, this work challenges the control theory explanation for the morphology of jerk CN as a slow drift from the target generated by a slow eye movement disorder, followed by a corrective saccade to refixate the target. The characteristic slow-fast form of jerk CN is instead attributed to the geometry of an underlying slow manifold in the saccadic system phase space.

Several implications of this work are in agreement with previous psychophysical investigations. The existence of a canard implies that once the system has developed a sustained oscillatory instability, the oscillation is likely to be a jerk, bidirectional jerk or pendular CN. This is consistent with the results of a recent study of oscillatory eye movement disorders [2]. Additionally, the mechanism by which dynamic overshoots are generated by the model suggest that the movements are caused by reversals of the saccadic control signal, as predicted by a previous study of the metrics of dynamic overshoots [12].

Finally, an outcome of this work which may have clinical implications is the suggestion that the transition from a jerk nystagmus to a bidirectional jerk nystagmus, which is often observed experimentally, may be a consequence of a gluing bifurcation. This implies the possibility of periodically forcing a target viewed by a jerk CN subject so as to bring the system close to homoclinicity, producing waveforms that give rise to lower retinal slip velocities, and hence to improved visual performance.

2 Oculomotor control, saccades and congenital nystagmus

2.1 Oculomotor control and saccades

In broad terms, the oculomotor system controls the movement of the eyes so as to ensure that the image of the object of interest falls on the region of the retina known as the fovea (a process referred to as foveation) [23]. Resolution of detail decreases sharply away from the fovea and is also degraded if images slip over the fovea at velocities greater than a few degrees per second. Consequently, optimal visual performance is only attained when images are held steady on this region [44].

Saccades are fast movements of the eye which bring about foveation of new targets [43]. The oculomotor subsystem responsible for the generation of horizontal saccades behaves in a very machine-like way. Experimental investigations of the dynamic characteristics of saccades have revealed that the peak velocity and duration of a saccade are related to its amplitude [43], [17]. This relationship is often referred to as the main sequence, and is used to classify an eye movement as a saccade [13].

A recording of a simple accurate (normometric) saccade is shown in figure 1-A. Normometric saccades often have a post-saccadic component referred to as a dynamic overshoot [34], [7]. A recorded dynamic overshoot is shown in figure 1-B. Inaccurate or dysmetric saccades can take the form of an initial undershoot (hypometric saccade) or overshoot (hypermetric saccade) of the desired eye position, resulting in a secondary corrective saccade [14].

Neurophysiological studies have shown that the saccadic control signal for horizontal saccades is generated by excitatory burst neurons in the brainstem. These are normally inhibited by omnipause neurons, except during a saccade, when the omnipause neurons cease firing. The firing rate of a burst neuron is a saturating nonlinear function of the dynamic motor error m, which is the difference between the required and current eye positions [42]. The burst neurons are divided into two types: right burst neurons which fire maximally for rightward saccades and left burst neurons which fire maximally for leftward saccades. The overall burst signal b can be expressed as the difference between the signals r and l from the right and left burst neurons respectively.

In addition to the response in the direction of maximal firing (the on-response), the burst neurons also have a small response in the opposite direction (the off-response). The off-response is believed to correspond to a small centripetal tug at the end of a small-amplitude movement that prevents the inertia of the eye causing overshoot of the target [42]. This will be referred to here as a braking signal. The effectiveness of the braking signal in slowing the eye at the end of the movement increases with the magnitude of the off-response. Evidence has also been found suggesting that burst neurons exhibit mutual inhibition, with the firing of right burst neurons suppressing that of left burst neurons, and vice versa [39].

According to the displacement feedback model of saccade generation illustrated in figure 2, saccades are produced in response to a desired gaze displacement signal Δg generated by higher brain centres [36]. In this scheme, the motor error m is obtained by subtracting an estimate s of current eye displacement from Δg. The burst signal b is sent to a complex of neurons in the brain stem, the neural integrator, which integrate it. The integrated signal n is then added to b, and the summed signal is relayed to the relevant ocular motoneurons. These send the final motor command to the eye muscles, which produce a shift in the eye position g. A copy of b is sent to a separate resettable integrator to generate the estimate s. The epithet 'resettable' refers to the fact that s is required to be set to 0 at the beginning of each saccade. This feedback model should act so as to drive m to 0, moving the eye to
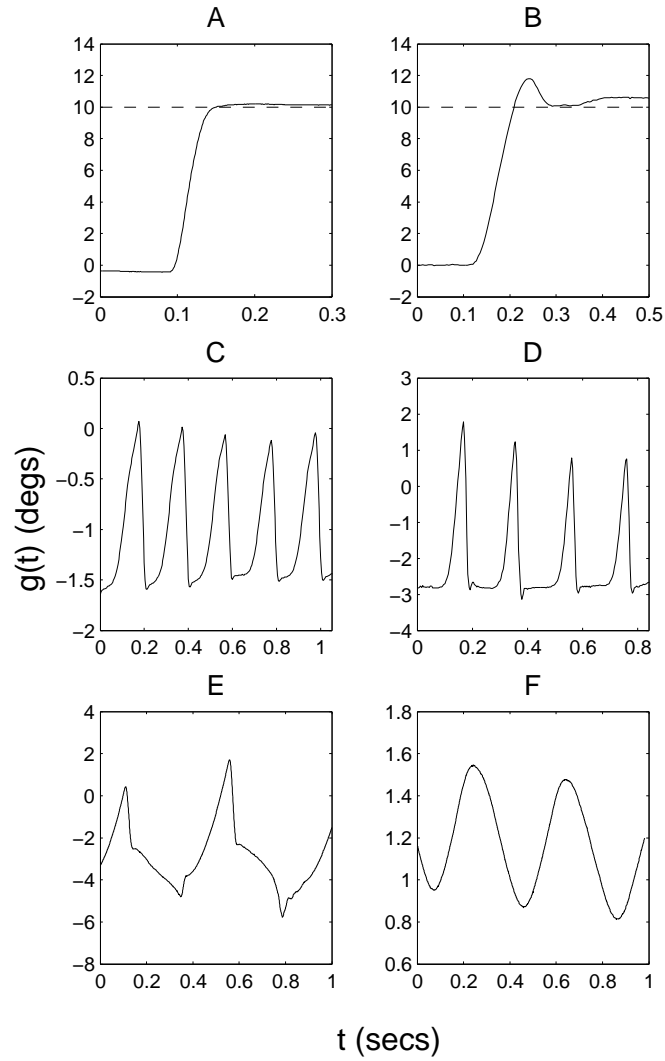
4

Figure 1: Recorded eye movements. t=time, $g(t)$=horizontal eye position, with $g(t) > 0$ corresponding to rightward gaze. A: normometric saccade. B: dynamic overshoot. C: left-beating jerk CN. D: jerk with extended foveation. E: bidirectional jerk. F: pendular CN. In A and B, the dotted line indicates the target position.
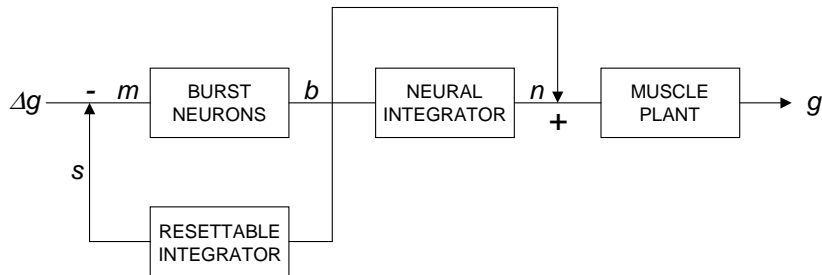
Figure 2: The displacement feedback model of saccade generation. A copy of the burst signal b is integrated to obtain an estimate of current eye displacement s which is fed back to generate the motor error m. g and n denote the gaze angle and integrated burst signal respectively. Δg denotes the required gaze displacement signal generated by higher brain centres, which initiates the saccade.

the required position $g(0) + \Delta g$. In control models of the oculomotor system, the ocular motoneurons and eye muscles are referred to collectively as the muscle plant.

2.2 Congenital nystagmus

CN is an involuntary, bilateral oscillation of the eyes that is present in approximately 1 in 4000 of the population [4]. The oscillations in each eye are strongly correlated, and occur primarily in the horizontal plane. In general, the retinal image is held on the fovea for a short time before a slow phase takes the target off the fovea. The slow phase is then interrupted by a fast or slow phase which moves the target directly onto the fovea [22], [4], [5]. As a consequence of the reduced foveation time, CN subjects tend to have poor visual acuity [6], [9], [16]. Some recordings of common CN waveforms are shown in figure 1. Jerk CN consists of an increasing exponential slow phase followed by a saccadic fast phase (fig. 1-C). The direction of the fast phase is referred to as the beat direction. Two variations on jerk are jerk with extended foveation, in which the eye spends a greater time in the vicinity of the foveation position (fig. 1-D), and bidirectional jerk, in which the eye beats alternately in both directions (fig. 1-E). The less common pendular nystagmus consists of sinusoidal slow phase movements (fig. 1-F).

Most CN subjects exhibit a range of different oscillations over a single recording period, with the particular waveform observed depending on factors such as gaze angle, attention and stress. In particular, it has been found that some subjects who exhibit a jerk nystagmus during a fixation task can switch to a pendular nystagmus upon entering a state of low attention, such as when closing their eyes or daydreaming [4], [5]. Many CN subjects have a gaze angle referred to as the neutral zone, in which the beat direction changes. Bidirectional oscillations can be observed close to the neutral zone [4].

6

3   A nonlinear dynamics model of the saccadic system

3.1   The model

The displacement feedback model of figure 2 can be described using the set of coupled ODEs below [18]:

$$\dot{g} = v \tag{1}$$

$$\dot{v} = -\left(\frac{1}{T_1} + \frac{1}{T_2}\right)v - \frac{1}{T_1 T_2}g + \frac{1}{T_1 T_2}n + \left(\frac{1}{T_1} + \frac{1}{T_2}\right)(r - l) \tag{2}$$

$$\dot{n} = -\frac{1}{T_N}n + (r - l) \tag{3}$$

$$\dot{r} = \frac{1}{\epsilon}\left(-r - \gamma r l^2 + F(m)\right) \tag{4}$$

$$\dot{l} = \frac{1}{\epsilon}\left(-l - \gamma l r^2 + F(-m)\right) \tag{5}$$

$$\dot{m} = -(r - l). \tag{6}$$

Equations (1) and (2) model the response of the muscle plant to the signals generated by the burst neurons. Here, g represents the eye position and v the eye velocity. These equations are based on quantitative investigations of physical eye movements which show that the muscle plant can be modelled as a second-order linear system with a slow time constant $T_1 = 0.15s$ and a fast time constant $T_2 = 0.012s$ [33]. (3) is the equation for n, the signal from the neural integrator. The slow time constant $T_N = 25s$ corresponds to the slow post-saccadic drift back to zero degrees observed experimentally [15].

(4) and (5) are the equations for the activities r and l of the right and left burst neurons. The function $F(m)$ defined by

$$F(m) = \begin{cases} \alpha'\left(1 - e^{-m/\beta'}\right) & \text{if } m \geq 0 \\ -\frac{\alpha}{\beta}m e^{m/\beta} & \text{if } m < 0 \end{cases} \tag{7}$$

models the response of the burst neurons to the motor error signal m. The form of $F(m)$ is based on the results of single-cell recordings from alert monkeys [42]. A schematic plot of $F(m)$ is shown in figure 3.

The function has four positive parameters, α', β', α and β which govern the forms of the modelled on- and off- responses. For $m \geq 0$, $F(m)$ is increasing, with $F(m) \to \alpha'$ as $m \to \infty$. Also, $F(\beta') = \alpha'\left(1 - e^{-1}\right)$. α' therefore determines the value at which the modelled on-response saturates as $m \to \infty$, and β' determines how quickly the saturation occurs. For $m < 0$, $F(m)$ has a single global maximum at $\left(-\beta, \frac{\alpha}{e}\right)$, and converges monotonically to 0 as $m \to -\infty$ from $-\beta$. α thus determines the magnitude of the modelled off-response, and hence the strength of the corresponding braking signal. β determines the motor error range over which a significant off-response occurs, and therefore the range for which there is effective braking.
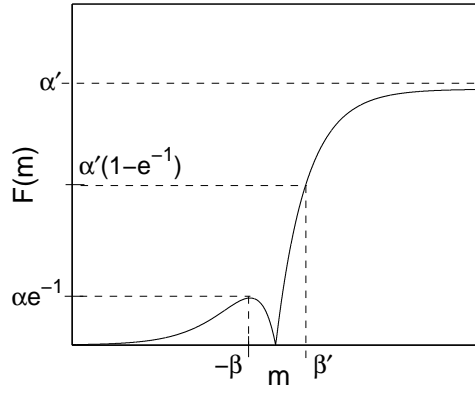
Figure 3: Schematic of the function $F(m)$ used to model the response curve for a saccadic burst neuron. The parameters α' and β' determine the modelled on-response while α and β determine the modelled off-response.

The terms $\gamma r l^2$ and $\gamma l r^2$ represent the mutual inhibition between the left and right burst neurons, with the parameter γ determining the strength of the inhibition. ϵ is a parameter which determines how quickly the neurons respond to the motor error signal m with the response time decreasing as ϵ is decreased. (6) is the equation for the resettable integrator, obtained by substituting $m = \Delta g - s$ into $\dot{s} = b$. Note that it is assumed that the resettable integrator is a perfect integrator, in contrast to the neural integrator which is leaky.

The parameters α', β' and γ are fixed at $\alpha' = 600$, $\beta' = 9$ and $\gamma = 0.05$, on the basis that these values give simulated saccades which lie on the main sequence [18]. The variable parameters of the model are thus α, β and ϵ, representing the off-response magnitude, off-response range and burst neuron response time respectively.

It should be noted that although the omnipause neurons are not explicitly included in the model, the burst neuron response function $F(m)$ implicitly incorporates the effects of both the burst neurons and the omnipause neurons. The omnipause neurons are active during the end of a saccade when they fire in order to bring the saccade to a stop, and therefore contribute to the form of $F(m)$ about $m = 0$.

3.2   Characterisation of the model as a skew-product

By setting $\mathbf{x} = (g, v, n)^T$ and $\mathbf{y} = (r, l, m)^T$, the system can be written in the skew-product form

$$\dot{\mathbf{x}} = A\mathbf{x} + B\mathbf{y}$$
$$\dot{\mathbf{y}} = \mathbf{G}(\mathbf{y}),$$

8

where A and B are the constant matrices

$$A = \begin{pmatrix} 0 & 1 & 0 \\ -\frac{1}{T_1 T_2} & -\left(\frac{1}{T_1} + \frac{1}{T_2}\right) & \frac{1}{T_1 T_2} \\ 0 & 0 & -\frac{1}{T_N} \end{pmatrix}, B = \begin{pmatrix} 0 & 0 & 0 \\ \frac{1}{T_1} + \frac{1}{T_2} & -\left(\frac{1}{T_1} + \frac{1}{T_2}\right) & 0 \\ 1 & -1 & 0 \end{pmatrix},$$

and $\mathbf{G}(\mathbf{y})$ represents the vector field of equations (4)-(6). Sometimes, for convenience, this notation will be condensed further by writing $\mathbf{z} = (\mathbf{x}, \mathbf{y})$ and $\dot{\mathbf{z}} = \mathbf{F}(\mathbf{z})$, where $\mathbf{F}(\mathbf{z}) = (A\mathbf{x} + B\mathbf{y}, \mathbf{G}(\mathbf{y}))$. Here, the fibre equations $\dot{\mathbf{x}} = A\mathbf{x} + B\mathbf{y}$ represent the muscle plant and neural integrator dynamics, while the base equations $\dot{\mathbf{y}} = \mathbf{G}(\mathbf{y})$ represent the dynamics of the burst neurons and resettable integrator. The base equations will be referred to collectively from now on as the burst equations. The skew-product form essentially enables the analysis of the full 6-dimensional system to be reduced to that of the 3-dimensional burst equations, as will now be discussed.

$F(m)$ is piecewise smooth about $m = 0$, from which it follows that $\mathbf{G}(\mathbf{y})$ is piecewise smooth about the set $\{\mathbf{y} \in \mathbb{R}^3 : m = 0\}$. Also, it is easy to see that $F(m)$ is locally Lipschitz on $\mathbb{R}$, and therefore that $\mathbf{F}(\mathbf{z})$ is locally Lipschitz on $\mathbb{R}^6$. Solutions of $\dot{\mathbf{z}} = \mathbf{F}(\mathbf{z})$ are therefore unique with respect to initial conditions [31]. Writing φ_t for the time t map of $\dot{\mathbf{y}} = \mathbf{G}(\mathbf{y})$ and ψ_t for the time t map of $\dot{\mathbf{z}} = \mathbf{F}(\mathbf{z})$, integration of the fibre equations implies that

$$\psi_t(\mathbf{z}) = \begin{pmatrix} e^{At}\mathbf{x} + \int_0^t e^{A(t-s)} B\varphi_s(\mathbf{y})\, ds \\ \varphi_t(\mathbf{y}) \end{pmatrix}.$$

The eigenvalues of e^{At} are $\left\{ e^{-\frac{t}{T_1}}, e^{-\frac{t}{T_2}}, e^{-\frac{t}{T_N}} \right\}$, all of which lie inside the unit circle for $t > 0$. Under the reasonable assumption that there is an invariant compact subset C of $\mathbb{R}^3$ such that all trajectories of $\dot{\mathbf{y}} = \mathbf{G}(\mathbf{y})$ are forward asymptotic to C, it follows from the form of $\psi_t(\mathbf{z})$ that there is a continuous function $h : \mathbb{R}^3 \rightarrow \mathbb{R}^3$ that has two important properties. First, the graph of h, $\{(h(\mathbf{y}), \mathbf{y}) : \mathbf{y} \in \mathbb{R}^3\}$, is invariant and attracting in $\dot{\mathbf{z}} = \mathbf{F}(\mathbf{z})$. Secondly, the homeomorphism $H : \mathbf{y} \longmapsto (h(\mathbf{y}), \mathbf{y})$ conjugates the time t maps φ_t and ψ_t on C (i.e. $(H \circ \varphi_t)(\mathbf{y}) = (\psi_t \circ H)(\mathbf{y})$ for $\mathbf{y} \in C$, $t \geq 0$) [40]. This implies that, asymptotically, the burst system $\dot{\mathbf{y}} = \mathbf{G}(\mathbf{y})$ and the full system $\dot{\mathbf{z}} = \mathbf{F}(\mathbf{z})$ are topologically equivalent. The asymptotic qualitative behaviour of the full system is therefore determined by that of the burst system. In particular, stable fixed points and stable limit cycles of the burst system correspond to stable fixed points and stable limit cycles respectively of the full system.

3.3 Relating $g(t)$ to $m(t)$

The ultimate object of interest is the gaze time series $\{g(t) : t \geq 0\}$ for initial condition with $v(0) = 0$, $n(0) = g(0)$ and $m(0) = \Delta g$, as this simulates a saccade of Δg degrees from an initial gaze angle of $g(0)$. The topological equivalence between the burst system and the full system imposes a relatively weak relationship between $g(t)$ and $m(t)$. A stronger

relationship can be obtained by utilising the linearity of the fibre equations in $\mathbf{x}$, enabling the morphology of $g(t)$ to be inferred from that of $m(t)$, when the attractors of the model are fixed points or limit cycles. This in turn allows the form of the simulated eye movement to be related directly to the corresponding attractor of the burst equations in these cases.

Introducing Laplace transforms and the specified initial conditions it is possible to show that

$$g(t) = g(0) R(t) + (g(0) + \Delta g) S(t) + (u_g * m)(t), \tag{8}$$

where

$$R(t) = \frac{1}{T_1 - T_2} \left(T_1 e^{-\frac{t}{T_2}} - T_2 e^{-\frac{t}{T_1}} \right) \tag{9}$$

$$S(t) = K_1 T_1 e^{-\frac{t}{T_1}} + K_2 T_2 e^{-\frac{t}{T_2}} + K_N T_N e^{-\frac{t}{T_N}} \tag{10}$$

$$u_g(t) = K_1 e^{-\frac{t}{T_1}} + K_2 e^{-\frac{t}{T_2}} + K_N e^{-\frac{t}{T_N}}, \tag{11}$$

with the constants K_1, K_2, K_N given by

$$K_1 = \frac{T_1^2 + T_2(T_1 - T_N)}{T_1(T_1 - T_2)(T_1 - T_N)}$$

$$K_2 = \frac{T_1(T_N - T_2) - T_2^2}{T_2(T_1 - T_2)(T_2 - T_N)}$$

$$K_N = \frac{T_N^2}{T_N(T_1 - T_N)(T_2 - T_N)}.$$

In terms of the response function

$$T_g(s) = \frac{-s\left(\left(\frac{1}{T_1} + \frac{1}{T_2}\right)s + \left(\frac{1}{T_1 T_N} + \frac{1}{T_2 T_N} + \frac{1}{T_1 T_2}\right)\right)}{\left(s + \frac{1}{T_1}\right)\left(s + \frac{1}{T_2}\right)\left(s + \frac{1}{T_N}\right)} \tag{12}$$

of the linear system (8), $S(t)$ and $u_g(t)$ can be written succinctly as:

$$S(t) = \mathcal{L}^{-1}\left[-\frac{T_g(s)}{s}\right] \tag{13}$$

$$u_g(t) = \mathcal{L}^{-1}[T_g(s)]. \tag{14}$$

(In the above expressions, $*$ represents Laplace convolution while $\mathcal{L}^{-1}$ denotes the inverse Laplace transform).

In practise, there are simple approximations to these quantities which are valid for physiologically realistic values of the parameters. Using the known values of T_1, T_2 and T_N gives

$$|T_2(T_1 - T_N)| \gg T_1^2$$

$$|T_1(T_N - T_2)| \gg T_2^2$$
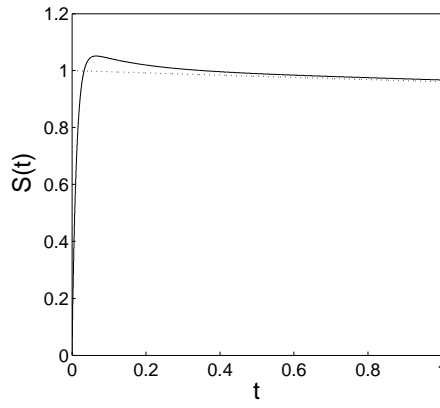
$$T_N \gg T_1, T_2,$$

Figure 4: Plot of the function $S(t)$ defined in (10). The function $e^{-\frac{t}{T_N}}$ is also shown (dotted line).

from which it follows that $K_1 T_1 \approx \frac{T_2}{T_1 - T_2}$, $K_2 T_2 \approx -\frac{T_1}{T_1 - T_2}$ and $K_N T_N \approx 1$. (9) and (10) therefore give the following approximation for $R(t)$:

$$R(t) \approx -S(t) + e^{-\frac{t}{T_N}}.$$

Substituting this into (8) implies

$$g(t) \approx g(0) e^{-\frac{t}{T_N}} + (\Delta g) S(t) + (u_g * m)(t). \tag{15}$$

Thus, to a good approximation, the simulated eye movement decomposes into two parts. The first two terms of (15) are independent of the error signal $m(t)$. Figure 4 is a plot of $S(t)$ for $t \geq 0$. It can be seen that $S(t)$ tends quickly to 1 before converging to 0 like $e^{-\frac{t}{T_N}}$. Taken together, the first two terms of (15) therefore approximate a saccade of Δg degrees from $g(0)$. The remaining term shows how the form of the error term $m(t)$ modifies this basic saccade.

In the case where the attractor of the burst equations is a fixed point, then the motor error $m(t) \to m_*$ for some $m_* \in \mathbb{R}$ as $t \to \infty$. Introducing the transient motor error $m_T(t) = m(t) - m_*$ and using (13)-(14) leads to

$$g(t) \approx g(0) e^{-\frac{t}{T_N}} + (\Delta g - m_*) S(t) + (u_g * m_T)(t). \tag{16}$$

(16) and the form of $S(t)$ suggest that if $|\Delta g|$ is large compared to $|m_*|$ and $m(t) \to m_*$ sufficiently fast as $t \to \infty$, then $g(t)$ will have the form of an accurate saccade to $g(0) + \Delta g$ which drifts back to 0 like $(g(0) + \Delta g) e^{-\frac{t}{T_N}}$. In this case, the equations model a normal saccadic control system. Clearly, if either of these conditions is violated, inaccurate or abnormal saccades will result. In particular, oscillations in $m(t)$ may induce oscillations in $g(t)$.

In the case where the attractor of the burst equations is a limit cycle of period T, the motor error $m(t)$ will converge to a periodic function $m_S(t)$. Similarly the gaze angle
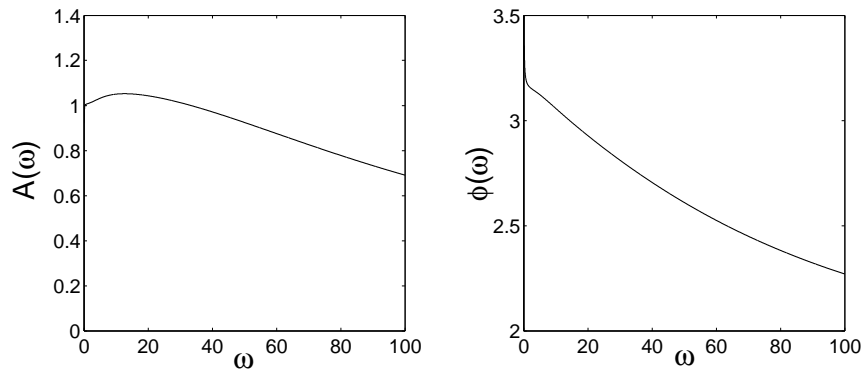
11

Figure 5: Plots of the amplitude variable $A(\omega)$ and phase variable $\phi(\omega)$ of the linear filter $T_g(i\omega)$ defined in (12) on the range $(0, 100)$.

$g(t)$ will converge to a periodic function $g_S(t)$ which (because of the linearity of the fibre dynamics) also has period T. Moreover, writing $m_S(t)$ as the Fourier series

$$m_S(t) = \sum_{k=-\infty}^{\infty} m_k^S e^{ik\omega_T t}$$

where $\omega_T = \frac{2\pi}{T}$, ignoring transients and using the linearity of the convolution implies that $g_S(t)$ has the Fourier series

$$g_S(t) = \sum_{k=-\infty}^{\infty} T_g(ik\omega_T) m_k^S e^{ik\omega_T t}$$

[32]. This is, in effect, a linear filtering of the time series $\{m_S(t) : t \geq 0\}$, where $T_g(i\omega)$ is the response function of the filter.

It is useful to write $T_g(i\omega)$ in terms of amplitude and phase variables, $T_g(i\omega) = A(\omega)e^{\phi(\omega)i}$. Explicit expressions for $A(\omega)$ and $\phi(\omega)$ in terms of the time constants T_1, T_2 and T_N can be obtained, but these are rather uninformative. Figure 5 shows plots of numerical evaluations of $A(\omega)$ and $\phi(\omega)$ for $0 < \omega < 100$. It is clear that $A(\omega)$ depends rather weakly on frequency in this range. Indeed, if ω is restricted to the interval $0.08 < \omega < 55$, then $|A(\omega) - 1| < 0.1$. In the same frequency range, the phase varies approximately linearly. A linear regression of $\phi(\omega)$ over this range implies that $\phi(\omega) \approx -t_g\omega + \pi$, where $t_g = 0.0115$. Taken together, these expressions for the amplitude and phase suggest the approximation $T_g(i\omega) \approx -e^{-t_g\omega i}$ for $0.08 < \omega < 55$.

If it is assumed that the periodic function $m_S(t) - \langle m_S(t) \rangle$ (where $\langle m_S(t) \rangle = \frac{1}{T}\int_0^T m_S(t)\,dt$) does not have significant energy outside the frequency range $0.08 < \omega < 55$, then setting $W_S = \{k \in \mathbb{Z} : 0.08 < |k\omega_T| < 55\}$ gives the approximation

$$m_S(t) - \langle m_S(t) \rangle \approx \sum_{k \in W_S} m_k^S e^{ik\omega_T t}. \tag{17}$$

As $|T_g(i\omega)| \approx 1$ for $\omega \in (0.08, 55)$ and $|T_g(i\omega)| < 1$ for $\omega \notin (0.08, 55)$ with $T_g(0) = 0$, it follows that $g_S(t)$ will also not have significant energy outside the frequency range

12

$0.08 < \omega < 55$. This leads to the approximation

$$g_S(t) \approx \sum_{k \in W_S} T_g(ik\omega_T) m_k^S e^{ik\omega_T t}.$$

Substituting $T_g(i\omega) \approx -e^{-t_g \omega i}$ into the above then gives

$$g_S(t) \approx - \sum_{k \in W_S} m_k^S e^{ik\omega_T(t-t_g)}.$$

Using (17) leads to the final approximation

$$g_S(t) \approx -m_S(t - t_g) + \langle m_S(t) \rangle. \tag{18}$$

Given this final approximation, $g(t)$ has the form of a saccade which decays to the periodic oscillation $g_S(t)$ as $t \to \infty$, where the morphology of $g_S(t)$ is determined by that of $m_S(t)$. The equations therefore model a pathological saccadic system with an asymptotically periodic oscillatory instability, the form of which is determined by that of the corresponding periodic motor error time series.

4 Analysis of the burst equations

It has been established in the previous sections that the asymptotic qualitative dynamics - and even quantitative dynamics - of the full model are determined by that of the burst equations $\dot{\mathbf{y}} = \mathbf{G}(\mathbf{y})$ given explicitly by

$$
\begin{align}
\dot{r} &= \frac{1}{\epsilon}\left(-r - \gamma r l^2 + F(m)\right) \tag{19}\\
\dot{l} &= \frac{1}{\epsilon}\left(-l - \gamma l r^2 + F(-m)\right) \tag{20}\\
\dot{m} &= -(r - l), \tag{21}
\end{align}
$$

where $F(m) = F(m; \alpha, \beta)$ is defined in (7). Before the bifurcation analysis of the burst equations is presented in 4.2, some general properties of the equations which aid their analysis - such as the existence of a symmetry - are discussed

4.1 General properties of the burst equations

4.1.1 Symmetry

The vector field $\mathbf{G}(\mathbf{y})$ is equivariant under the action of the group $\mathbb{Z}_2 = \{id, \sigma\}$, where σ acts linearly on $\mathbb{R}^3$ according to $\sigma : (r, l, m) \longmapsto (l, r, -m)$. If follows that σ maps trajectories of $\dot{\mathbf{y}} = \mathbf{G}(\mathbf{y})$ into each other, and that the set L_0 defined by $L_0 = \{\mathbf{y} \in \mathbb{R}^3 : \sigma \mathbf{y} = \mathbf{y}\}$ is invariant under the dynamics [27]. L_0 is given explicitly by
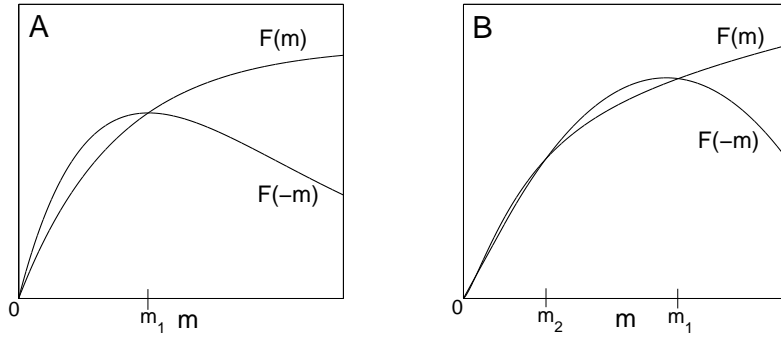
$$L_0 = \left\{(x, x, 0)^T : x \in \mathbb{R}\right\}.$$

Figure 6: Schematic of the possible intersections of the functions $F(m)$ and $F(-m)$ on the positive real line.

Restricting the vector field to L_0 gives the following first order system:

$$\dot{x} = -\left(1 + \gamma x^2\right) x. \tag{22}$$

The point $x = 0$, the unique attracting fixed point of (22), corresponds to a fixed point at the origin $\mathbf{0} = (0, 0, 0)^T$ of the full system. The invariance of L_0 therefore implies that it is a 1-dimensional stable manifold of the origin. Since this property is a consequence of the symmetry, the existence and form of this stable manifold do not depend on the model parameters α, β and ϵ.

4.1.2 Fixed points

The existence of the symmetry σ implies that invariant sets of the equations are either symmetry invariant, or form pairs related by the action of σ. In particular, fixed points of (19)-(21) have the form $(r_*, r_*, \pm m_*)^T$, where m_* - which will be taken to be nonnegative - solves $F(m) = F(-m)$, and $r_* \geq 0$ is the unique real solution to $\gamma r^3 + r - F(m_*) = 0$. Consideration of the form of $F(m)$ shows that 0 is always a solution of $F(m) = F(-m)$ which gives rise to the fixed point at the origin. Nontrivial solutions of $F(m) = F(-m)$ on $\mathbb{R}^+$ can occur generically in one of two ways depending on the shape of the function $F(m)$, as illustrated in figure 6.

Much of this can be understood in terms of the right and left derivatives of $F(m)$ at $m = 0$. Write Λ_+ for $\lim_{m \to 0+} DF(m) = \frac{\alpha'}{\beta'}$ and Λ_- for $\lim_{m \to 0-} DF(m) = -\frac{\alpha}{\beta}$. Then as suggested by figure 6-A, for $\alpha > \Lambda_+ \beta$ (that is for $-\Lambda_- > \Lambda_+$), there is a single nontrivial solution m_1 of $F(m) = F(-m)$ on $\mathbb{R}^+$. For $\alpha < \Lambda_+ \beta$ (that is for $-\Lambda_- < \Lambda_+$), there are two possibilities. For some values of β, $F(m)$ can intersect $F(-m)$ tangentially as α is increased from 0 in this range. For such β values, there is a critical value of α at which the tangency occurs; this will be written as $T(\beta)$. It then follows that there are no nontrivial solutions of $F(m) = F(-m)$ on $\mathbb{R}^+$ for $\alpha < T(\beta)$, a single solution m_1 for $\alpha = T(\beta)$, and a pair of nontrivial solutions $\{m_1, m_2\}$ for $T(\beta) < \alpha < \Lambda_+ \beta$ (see figure 6-B). The convention will be that m_1 and m_2 are labelled so that $m_2 < m_1$. For β values such that
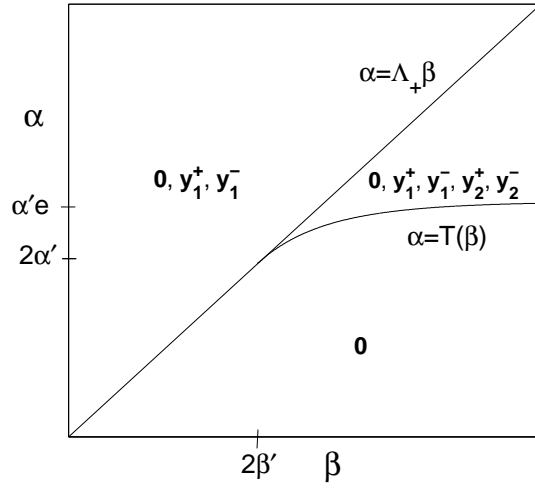
14

Figure 7: Schematic plots of the curves $\alpha = \Lambda_+ \beta$ and $\alpha = T(\beta)$ in the (β, α) plane. The fixed points of the burst equations in each region of the (β, α) plane are also indicated. **0** represents the fixed point at the origin, $(0,0,0)^T$. $\mathbf{y}_i^+$ and $\mathbf{y}_i^-$ have the forms $(r_i, r_i, m_i)^T$ and $(r_i, r_i, -m_i)^T$ respectively, where $m_i > 0$ solves $F(m) = F(-m)$ and $r_i > 0$ solves $\gamma r_i^3 + r_i - F(m_i) = 0$.

no tangential intersection of $F(m)$ and $F(-m)$ can occur when $\alpha < \Lambda_+ \beta$, there are no nontrivial solutions of $F(m) = F(-m)$ on $\mathbb{R}^+$ in this range.

$T(\beta)$ is defined parametrically in terms of m_1 as below:

$$\beta = \frac{\beta' m_1 \left(1 - e^{m_1/\beta'}\right)}{\beta' \left(1 - e^{m_1/\beta'}\right) + m_1}$$

$$T(\beta) = \frac{\alpha' \beta(m_1) e^{m_1/\beta(m_1)}}{\beta' + m_1 \left(1 - \frac{\beta'}{\beta(m_1)}\right)}.$$

By considering the limit $m_1 \to 0$ in this parametric representation, it can be shown that tangential intersections can only occur for $\beta > 2\beta'$; that is $T(\beta)$ is only defined in this range. Moreover, in the (β, α) plane, the curve $\alpha = T(\beta)$ converges tangentially to the line $\alpha = \Lambda_+ \beta$ as $\beta \to 2\beta'+$. By considering the limit $m_1 \to \infty$, it can be deduced that the curve $\alpha = T(\beta)$ asymptotes to the line $\alpha = \alpha' e$ as $\beta \to \infty$, with $T(\beta)$ strictly increasing on $(2\beta', \infty)$.

This discussion is summarised in figure 7 which shows a schematic of the curves $\alpha = T(\beta)$ and $\alpha = \Lambda_+ \beta$ in the (β, α) plane. Also shown are the fixed points of $\dot{\mathbf{y}} = \mathbf{G}(\mathbf{y})$, where for a given nontrivial solution m_i of $F(m) = F(-m)$ on $\mathbb{R}^+$, the corresponding fixed points are written as $\mathbf{y}_i^+ = (r_i, r_i, m_i)^T$ and $\mathbf{y}_i^- = (r_i, r_i, -m_i)^T$. Figure 7 suggests that $(2\beta', 2\alpha')$ is a codimension 2 point at which a line of nonsmooth pitchfork-type bifurcations at the origin intersects a line of symmetry-related saddlenode bifurcations.[1]

---

[1]The bifurcation at the origin which occurs as α increases through $\Lambda_+ \beta$ is not a standard pitchfork bifurcation as the vector field $\mathbf{G}$ is not smooth at **0**.

15

4.1.3 Slow manifold

For small ϵ, the burst equations are a slow-fast system [46]. The associated slow manifold, which will be written S_M, is the union of curves given by the intersection of the r- and l-nullclines. Trajectories contract onto S_M parallel to the (r, l) plane and then evolve on S_M according to the equation $\dot{m} = -(r - l)$. Trajectories on S_M therefore move along it in the positive m direction for $r < l$ and in the negative m direction for $r > l$. As ϵ is decreased, trajectories contract onto the slow manifold more quickly and follow it more closely. It can be seen from (19)-(20) that S_M is independent of ϵ, and is invariant under σ.

A more detailed understanding of the geometric form of S_M can be obtained by considering its parameterised form

$$\left\{ \left(\frac{F(m)}{1 + \gamma l_M(m)^2}, l_M(m), m \right)^T : m \in \mathbb{R} \right\}, \tag{23}$$

where $l_M(m)$ solves $G_M(l; m) = 0$, with $G_M(l; m)$ given by

$$G_M(l; m) = l^5 - F(-m) l^4 + \frac{2}{\gamma} l^3 - \frac{2F(-m)}{\gamma} l^2 + \frac{1}{\gamma} \left(F(m)^2 + \frac{1}{\gamma} \right) l - \frac{F(-m)}{\gamma^2}.$$

Consider foliating the phase space with planes of constant m. For a given value m' of m, since $G_M(l; m)$ is a quintic polynomial in l, S_M intersects the plane $m = m'$ generically at 1, 3 or 5 points. Moreover, there is always at least one point of intersection. It follows that in (r, l, m) space, S_M always contains at least one curve, which will be written as S_1. As m is varied, new points of intersection are generated through the quintic $G_M(l; m)$ developing pairs of additional roots.

Something of the structure of S_M can be understood by considering various limits of m. As $m \to 0$, $F(m) \to 0$, and so $G_M(l; m) \to l \left(l^2 + \frac{1}{\gamma} \right)^2$. This function has only one real root at $l = 0$, and (23) implies that this root corresponds to the origin $\mathbf{0}$, which always lies on S_M. It follows that for small $|m|$, $S_M = S_1$ with $S_1 \to \mathbf{0}$ as $m \to 0$.

Considering the limit as $m \to \infty$, $F(m) \to \alpha'$ and $F(-m) \to 0$, from which it follows that $G_M(l; m) \to l \left(l^4 + \frac{2}{\gamma} l^2 + \frac{1}{\gamma} \left((\alpha')^2 + \frac{1}{\gamma} \right) \right)$. Again, $l = 0$ is the only real root of this function implying that $S_M = S_1$ for $m > 0$ with m large. Moreover, (23) implies that S_1 converges to the curve $\left\{ (F(m), 0, m)^T : m > 0 \right\}$ as $m \to \infty$. By symmetry, $S_M = S_1$ for $m < 0$ with $|m|$ large. Indeed, S_1 converges to the curve $\left\{ (0, F(-m), m)^T : m < 0 \right\}$ as $m \to -\infty$, .

For intermediate values of $|m|$, S_1 may have turning points with respect to the m axis, while S_M may contain other curves in addition to S_1. As roots of $G_M(l; m)$ are created in pairs, any such additional curves will be closed loops. Examples of the form of S_M appear in figures 9, 12 and 14.

The existence of S_M restricts the behaviour of the burst equations for small ϵ. Firstly, since all attractors must have portions lying on S_M, and S_M is a 1-dimensional set, it is reasonable to assume that the only possible attractors are stable fixed points and stable

limit cycles. Secondly, trajectories cannot cross the $m = 0$ plane. This can be seen by noting that $S_M = S_1$ for $|m|$ small; any trajectory which crosses the plane must therefore do so on S_1, which cannot happen as S_1 contains a fixed point at the origin.

4.1.4 Smooth vector fields

In interpreting the bifurcations and local dynamics of the burst equations at the origin $\mathbf{0}$ where the vector field $\mathbf{G}$ is not smooth, it will be useful to consider the smooth vector fields $\mathbf{G}_+$ and $\mathbf{G}_-$ defined as follows:

$$\mathbf{G}_+ (r, l, m) = \begin{pmatrix} \frac{1}{\epsilon} \left(-r - \gamma r l^2 + \alpha' \left(1 - e^{-m/\beta'} \right) \right) \\ \frac{1}{\epsilon} \left(-l - \gamma l r^2 + \frac{\alpha}{\beta} m e^{-m/\beta} \right) \\ -(r - l) \end{pmatrix} \tag{24}$$

$$\mathbf{G}_- (r, l, m) = \begin{pmatrix} \frac{1}{\epsilon} \left(-r - \gamma r l^2 - \frac{\alpha}{\beta} m e^{m/\beta} \right) \\ \frac{1}{\epsilon} \left(-l - \gamma l r^2 + \alpha' \left(1 - e^{m/\beta'} \right) \right) \\ -(r - l) \end{pmatrix}. \tag{25}$$

These vector fields have been chosen so as to agree with $\mathbf{G}$ on the appropriate half-spaces: $\mathbf{G}_+|_{m\geq 0} = \mathbf{G}|_{m\geq 0}$ and $\mathbf{G}_-|_{m\leq 0} = \mathbf{G}|_{m\leq 0}$. Consequently, each trajectory of $\dot{\mathbf{y}} = \mathbf{G}(\mathbf{y})$ can be expressed as a union of sections of trajectories of $\dot{\mathbf{y}} = \mathbf{G}_+(\mathbf{y})$ and $\dot{\mathbf{y}} = \mathbf{G}_-(\mathbf{y})$. Also, $\sigma \circ \mathbf{G}_+ = \mathbf{G}_- \circ \sigma$, and so solutions of $\dot{\mathbf{y}} = \mathbf{G}_+(\mathbf{y})$ and $\dot{\mathbf{y}} = \mathbf{G}_-(\mathbf{y})$ map into each other under σ. As $\mathbf{G}_\pm|_{m=0} = \mathbf{G}|_{m=0}$, $\mathbf{0}$ is a fixed point of both smooth systems and L_0 is a stable manifold of $\mathbf{0}$, for all parameter values.

4.2 Bifurcations, attractors and simulated eye movements

The bifurcation analysis presented in this section is divided into two main parts. In 4.2.1, the bifurcations of the burst equations which occur as α and β are varied for a fixed small ϵ are described. These results provide the basis for 4.2.2, in which the restriction to small ϵ is lifted, and the bifurcations which occur in the reduced range $1.5 < \beta < 6$, $\alpha < \alpha'$ are considered. This reduced range contains the parameter values for which biologically realistic simulated eye movements were found during the initial numerical investigation of the full model presented in [18]. In 4.2.2, the morphology of each of these simulated eye movements is interpreted in terms of the corresponding attractor of the burst equations. The results of the section are summarised in figure 15.

4.2.1 Bifurcations and attractors for small ϵ

Figure 8 is a schematic diagram of the bifurcations and attractors of the burst equations for small ϵ. The figure was obtained by combining standard linear stability analysis with numerical work and the assumption that the equations have only fixed point and limit cycle
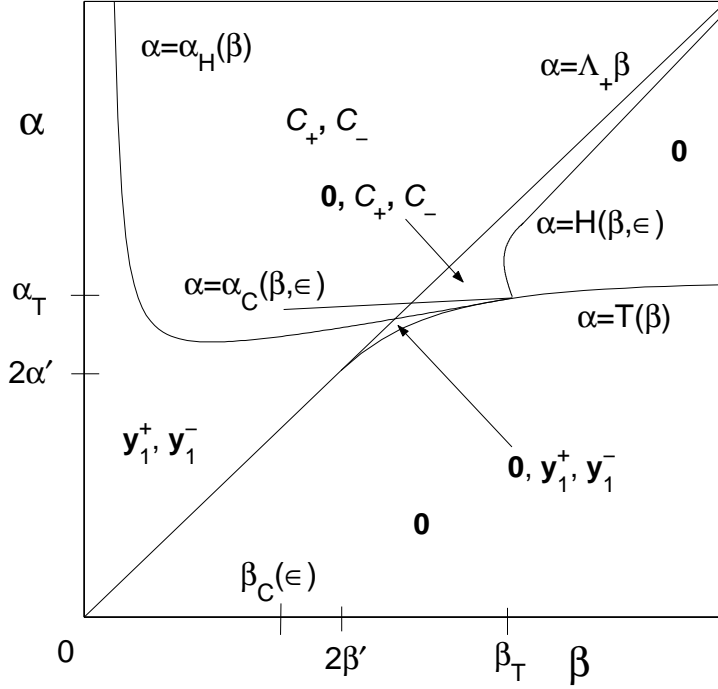
Figure 8: Bifurcations and attractors of the burst equations (4)-(6) for small ϵ. $\alpha = \Lambda_+\beta$ is a line of nonsmooth pitchfork bifurcations at the origin $\mathbf{0} = (0,0,0)^T$. The bifurcation is supercritical for $\beta < 2\beta'$, producing a pair of stable fixed points $\{\mathbf{y}_1^+, \mathbf{y}_1^-\}$, and subcritical for $\beta > 2\beta'$, destroying a pair of unstable fixed points $\{\mathbf{y}_2^+, \mathbf{y}_2^-\}$. $\alpha = T(\beta)$ is a line of symmetry-related saddlenode bifurcations. All fixed points $\{\mathbf{y}_1^+, \mathbf{y}_1^-, \mathbf{y}_2^+, \mathbf{y}_2^-\}$ produced by the bifurcations are unstable for $\beta > \beta_T$, while for $\beta < \beta_T$, $\{\mathbf{y}_1^+, \mathbf{y}_1^-\}$ are created stable and $\{\mathbf{y}_2^+, \mathbf{y}_2^-\}$ are created unstable. $\alpha = \alpha_H(\beta)$ is a line of symmetry-related supercritical Hopf bifurcations at $\mathbf{y}_1^+$ and $\mathbf{y}_1^-$ at which a pair of stable limit cycles $\{\mathcal{C}_+, \mathcal{C}_-\}$ are produced. $\alpha = H(\beta, \epsilon)$ is a curve of symmetry-related saddlenode homoclinic bifurcations at $\mathbf{y}_2^+$ and $\mathbf{y}_2^-$ which destroy $\mathcal{C}_+$ and $\mathcal{C}_-$. $\alpha = \alpha_C(\beta, \epsilon)$ is a line of symmetry-related Hopf-initiated canards at which $\mathcal{C}_+$ and $\mathcal{C}_-$ undergo a sudden increase in amplitude.

attractors for small ϵ.[2] The bifurcations are organised by a pair of codimension-two points. The first of these is the point $(2\beta', 2\alpha')$ identified in section 4.1.2. The second codimension-two point, labelled (β_T, α_T), is of the Takens-Bogdanov type. Each is discussed in turn below.

The codimension-two point $(2\beta', 2\alpha')$: At this point, a line $\alpha = T(\beta)$ of symmetry-related saddlenode bifurcations intersects a line $\alpha = \Lambda_+\beta$ of nonsmooth, pitchfork-type bifurcations involving the origin $\mathbf{0}$. For $\beta > \beta_T$, all fixed points $\{\mathbf{y}_1^+, \mathbf{y}_1^-, \mathbf{y}_2^+, \mathbf{y}_2^-\}$ created by the saddlenode bifurcations are unstable, while for $\beta < \beta_T$, $\{\mathbf{y}_1^+, \mathbf{y}_1^-\}$ are created stable and $\{\mathbf{y}_2^+, \mathbf{y}_2^-\}$ are created unstable (cf. figure 7). The pitchfork-type bifurcation can occur in two ways, depending on the sign of $\beta - 2\beta'$. For $\beta < 2\beta'$, the bifurcation is supercritical: as α increases through $\Lambda_+\beta$, $\mathbf{0}$ loses stability and a pair of stable fixed points $\{\mathbf{y}_1^+, \mathbf{y}_1^-\}$ is created. For $\beta > 2\beta'$, the bifurcation is subcritical: as α increases through $\Lambda_+\beta$, $\mathbf{0}$ loses stability and a pair of unstable fixed points $\{\mathbf{y}_2^+, \mathbf{y}_2^-\}$ is destroyed (cf. figure 7 again).

The pitchfork-type bifurcation can be understood in terms of standard transcritical and pitchfork bifurcations which occur in the smooth system $\dot{\mathbf{y}} = \mathbf{G}_+(\mathbf{y})$ defined in (24). It can be shown that given a fixed β and ϵ, for α with $|\alpha - \Lambda_+\beta|$ sufficiently small, the origin has a smooth, 1-dimensional, attracting local centre manifold W_C^+, which is tangential to the vector $(\Lambda_+, \Lambda_+, 1)^T$ at $\mathbf{0}$ when $\alpha = \Lambda_+\beta$. Moreover, the dynamics on W_C^+ is given by

$$\dot{z} = P(z, \alpha) = (\alpha - \Lambda_+\beta)\, z - \Lambda_+ a z^2 - \Lambda_+ \left(2\epsilon\Lambda_+ a^2 + b\right) z^3 + \hat{O}(3), \qquad (26)$$

where

$$z \;=\; -\epsilon r + \epsilon l + m \qquad (27)$$

$$a \;=\; \frac{1}{\beta} - \frac{1}{2\beta'} \qquad (28)$$

$$b \;=\; \frac{1}{6(\beta')^2} - \frac{1}{2\beta^2}, \qquad (29)$$

and $\hat{O}(3)$ represents all terms of the form $\left\{z^i (\alpha - \Lambda_+\beta)^j : i + j \geq 3\right\}$, excluding z^3 [10]. It then follows from the symmetry that for small ϵ, the set W_C defined by $W_C = \left(W_C^+ \cap \{\mathbf{y} : m \geq 0\}\right) \cup \left((\sigma W_C^+) \cap \{\mathbf{y} : m \leq 0\}\right)$ is a 1-dimensional, attracting local set of the piecewise smooth system $\dot{\mathbf{y}} = \mathbf{G}(\mathbf{y})$ containing $\mathbf{0}$, on which the dynamics is given by

$$\dot{z} = Q(z, \alpha) = \begin{cases} P(z, \alpha) & \text{if } z \geq 0 \\ -P(-z, \alpha) & \text{if } z \leq 0 \end{cases}. \qquad (30)$$

A fixed point $z_* \geq 0$ of the W_C^+ dynamics $\dot{z} = P(z, \alpha)$ gives rise to a pair of fixed points $\{z_*, -z_*\}$ of the W_C dynamics $\dot{z} = Q(z, \alpha)$. These in turn correspond to a pair of fixed

---

[2]Many of the bifurcation curves lie very close to each other in the (β, α) plane, and so a schematic plot has been given to aid visualisation.

points $\mathbf{y}_* = (r_*, r_*, z_*)^T$ and $\sigma \mathbf{y}_* = (r_*, r_*, -z_*)^T$ of $\dot{\mathbf{y}} = \mathbf{G}(\mathbf{y})$.[3] In particular, 0 is a fixed point of both the W_C^+ and W_C dynamics, corresponding to the fixed point of $\dot{\mathbf{y}} = \mathbf{G}(\mathbf{y})$ at $\mathbf{0}$. The stability of a fixed point $z_* \geq 0$ of $\dot{z} = P(z, \alpha)$ determines that of both z_* and $-z_*$ (as fixed points of $\dot{z} = Q(z, \alpha)$), and hence of $\mathbf{y}_*$ and $\sigma \mathbf{y}_*$.

Equation (26) can be thought of as an unfolding of the dynamics near a degenerate fixed point at $z = 0$. In the case where $\beta \neq 2\beta'$ (that is when $a \neq 0$), $P(z, \alpha)$ is equivalent to the normal form $P_N(z, \alpha) = (\alpha - \Lambda_+ \beta) z - \mathrm{sign}(a) z^2$. This family is well known to have a transcritical bifurcation at $\alpha = \Lambda_+ \beta$ [11]. For the full system, $\dot{z} = Q(z, \alpha)$, there are correspondingly two cases depending on the sign of a. When $\mathrm{sign}(a) > 0$ ($\beta < 2\beta'$), 0 loses stability as α is increased through $\Lambda_+ \beta$. This is a kind of supercritical bifurcation which involves only the nonnegative fixed points (and their images under $z \longmapsto -z$) of the transcritical normal form. The bifurcation creates two new stable fixed points $\{m_1, -m_1\}$. Superficially, this resembles a standard supercritical pitchfork bifurcation; however, m_1 scales like $\alpha - \Lambda_+ \beta$ rather than $\sqrt{\alpha - \Lambda_+ \beta}$. The case $\mathrm{sign}(a) < 0$ ($\beta > 2\beta'$) gives the corresponding subcritical bifurcation. As α is increased through $\Lambda_+ \beta$, 0 loses stability and a pair of unstable fixed points $\{m_2, -m_2\}$ is destroyed. Again, m_2 scales like $\alpha - \Lambda_+ \beta$.

When $\beta = 2\beta'$ (that is, when $a = 0$), the quadratic normal form is no longer valid. $P(z, \alpha)$ is instead equivalent to the normal form $P_N(z, \alpha) = (\alpha - \Lambda_+ \beta) z - z^3$. In contrast to the case $\beta \neq 2\beta'$, $-P(-z, \alpha) = P(z, \alpha)$, and so the full vector field $Q(z, \alpha)$ is also equivalent to this normal form. This family of smooth vector fields is well known to have a supercritical pitchfork bifurcation at $\alpha = \Lambda_+ \beta$ [11]. At this bifurcation, 0 loses stability creating the stable pair of fixed points $\{m_1, -m_1\}$.

The codimension-2 point (β_T, α_T): At this point, the Jacobian matrices $D\mathbf{G}\left(\mathbf{y}_1^+\right)$ and $D\mathbf{G}\left(\mathbf{y}_1^-\right)$ both have the normal form

$$
\begin{pmatrix}
-\frac{4}{\epsilon} & 0 & 0 \\
0 & 0 & 1 \\
0 & 0 & 0
\end{pmatrix},
$$

identifying (β_T, α_T) as a Takens-Bogdanov point [29]. (β_T, α_T) lies at the intersection of three curves: a curve $\alpha = \alpha_H(\beta)$ of symmetry-related supercritical Hopf bifurcations at $\mathbf{y}_1^+$ and $\mathbf{y}_1^-$; a curve $\alpha = H(\beta, \epsilon)$ of symmetry-related saddlenode homoclinic bifurcations at $\mathbf{y}_2^+$ and $\mathbf{y}_2^-$; and the curve $\alpha = T(\beta)$ representing the creation of $\{\mathbf{y}_1^+, \mathbf{y}_2^+\}$ and, by symmetry, $\{\mathbf{y}_1^-, \mathbf{y}_2^-\}$ through saddlenode bifurcations.

The limit cycles produced by the Hopf bifurcations at $\mathbf{y}_1^+$ and $\mathbf{y}_1^-$ will be referred to as $\mathcal{C}_+$ and $\mathcal{C}_-$ respectively. It was pointed out in 4.1.3 that for small ϵ, trajectories cannot cross the $m = 0$ plane. It therefore follows that $\mathcal{C}_+$ lies in $m > 0$ and $\mathcal{C}_-$ lies in $m < 0$. Moreover, since σ maps trajectories of the burst equations into each other, $\mathcal{C}_- = \sigma \mathcal{C}_+$. As

---

[3](27) implies that if $(r_*, r_*, m_*)^T$ is a fixed point of $\dot{\mathbf{y}} = \mathbf{G}(\mathbf{y})$ corresponding to z_*, then $m_* = z_*$.

can be seen in figure 8, $\mathcal{C}_+$ and $\mathcal{C}_-$ exist in the region of the (β, α) plane lying between the curves $\alpha = \alpha_H(\beta)$ and $\alpha = H(\beta, \epsilon)$. Crossing the curve $\alpha = H(\beta, \epsilon)$ from left to right in the (β, α) plane causes the limit cycle $\mathcal{C}_+$ to be destroyed in a homoclinic bifurcation at $\mathbf{y}_2^+$. Similarly, by symmetry, $\mathcal{C}_-$ is destroyed at $\mathbf{y}_2^-$.

The values β_T, α_T and the function $\alpha_H(\beta)$ are given explicitly by

$$\beta_T = \frac{2\beta' m_H}{2\beta' - m_H \left(\alpha' \sqrt{\bar{\gamma}} - 2\right)} \tag{31}$$

$$\alpha_T = \frac{2\beta_T e^{m_H/\beta_T}}{m_H \sqrt{\bar{\gamma}}} \tag{32}$$

$$\alpha_H(\beta) = \frac{2}{m_H \sqrt{\bar{\gamma}}} \beta e^{m_H/\beta}, \tag{33}$$

where

$$m_H = \ln \left(\frac{\alpha' \sqrt{\bar{\gamma}}}{\alpha' \sqrt{\bar{\gamma}} - 2} \right)^{\beta'} \tag{34}$$

is the value of m_1 at $\alpha = \alpha_H(\beta)$. α_T, β_T and m_H have the approximate numerical values $\alpha_T = 1203$, $\beta_T = 18.05$ and $m_H = 0.135$. Viewed as a graph in the (β, α) plane, the function $\alpha_H(\beta)$ has a global minimum at m_H, and increases without bound as $\beta \to 0$.

Numerical work indicates that for a given small ϵ, there is a value $\beta_C(\epsilon)$ of β such that $\mathcal{C}_+$ and $\mathcal{C}_-$ undergo a sudden increase in amplitude as α is increased from $\alpha_H(\beta)$ for a fixed β in the range $(\beta_C(\epsilon), \beta_T)$. This amplitude increase is characterised by a local maximum of the derivative $D_\alpha \rho(\alpha, \beta, \epsilon)$ of the function

$$\rho(\alpha, \beta, \epsilon) = \max_{(r,l,m)^T \in \mathcal{C}_+} \{m\} - \min_{(r,l,m)^T \in \mathcal{C}_+} \{m\},$$

which measures the extent of $\mathcal{C}_+$ (and by symmetry $\mathcal{C}_-$) in the m direction [10]. The value of α corresponding to the maximum of $D_\alpha \rho(\alpha, \beta, \epsilon)$ for a given β and ϵ is written as $\alpha_C(\beta, \epsilon)$. The amplitude increase at this value appears to be attributable to symmetry-related Hopf-initiated canards ([28]), in which $\mathcal{C}_+$ and $\mathcal{C}_-$ develop segments that lie on the slow manifold $S_M(\alpha, \beta)$ as α is increased [10].

The mechanism by which the canards occur is illustrated with an example in figure 9, which shows the evolution of $\mathcal{C}_+$ and S_M in the region $m > 0$ as α is increased for $\beta = 0.75$, $\epsilon = 0.001$ (the corresponding evolution of $\mathcal{C}_-$ and S_M in the region $m < 0$ can be inferred from the symmetry). For $\alpha > \alpha_H(\beta)$ with $|\alpha - \alpha_H(\beta)|$ sufficiently small, $S_M \cap \{\mathbf{y} : m > 0\}$ consists of the curve S_1 together with a closed curve S_+. The limit cycle $\mathcal{C}_+$ is restricted to S_1, and does not interact with S_+ (see fig. 9-A). As α is increased from $\alpha_H(\beta)$ through some critical value $\bar{\alpha}_C(\beta)$, S_+ and S_1 merge, forming a single curve. For $\alpha > \bar{\alpha}_C(\beta)$, $\mathcal{C}_+$ has portions lying on the region of S_1 formed by the merging with S_+. The rapid increase in the amplitude of $\mathcal{C}_+$ as α increases through $\alpha_C(\beta, \epsilon)$ corresponds to the subset of this region lying between the origin and the point with largest m value becoming attracting (see figures 9-B and 9-C). The post-canard limit cycles $\{\mathcal{C}_+, \mathcal{C}_-\}$ have the form of a relaxation oscillation.
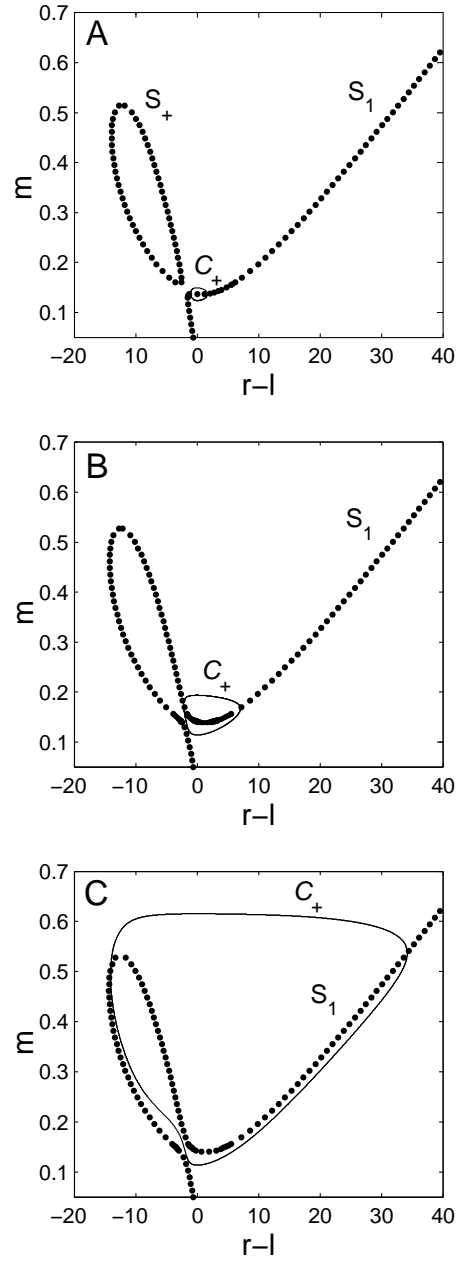
Figure 9: Projection into the $(r-l, m)$ plane of the Hopf-initiated canard involving $\mathcal{C}_+$ which occurs in the burst equations for $\beta = 0.75$, $\epsilon = 0.001$. A: $\alpha_H(\beta) < \alpha = 59.5328 < \bar{\alpha}_C(\beta)$. B: $\bar{\alpha}_C(\beta) < \alpha = 59.8486 < \alpha_C(\beta, \epsilon)$. C: $\alpha = 59.9539 > \alpha_C(\beta, \epsilon)$. The dotted line indicates the slow manifold S_M.
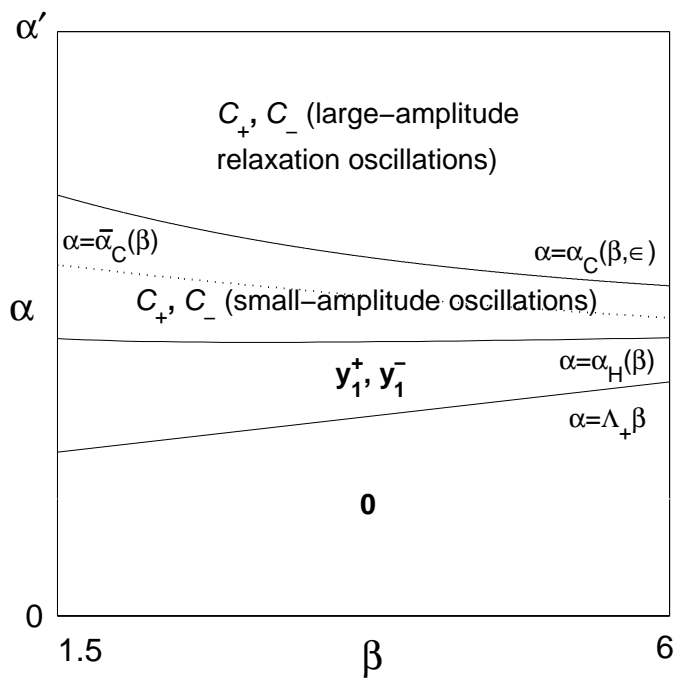
Figure 10: Bifurcations and attractors of the burst equations for $1.5 < \beta < 6$, $\alpha < \alpha'$ and ϵ small. $\alpha = \Lambda_+ \beta$ is a line of supercritical nonsmooth pitchfork bifurcations at the origin $\mathbf{0} = (0,0,0)^T$ which creates the stable fixed points $\{\mathbf{y}_1^+, \mathbf{y}_1^-\}$. $\alpha = \alpha_H (\beta)$ is a line of symmetry-related supercritical Hopf bifurcations at $\{\mathbf{y}_1^+, \mathbf{y}_1^-\}$ which creates the stable limit cycles $\{\mathcal{C}_+, \mathcal{C}_-\}$. $\alpha = \alpha_C (\beta, \epsilon)$ is a line of symmetry-related Hopf-initiated canards involving $\mathcal{C}_+$ and $\mathcal{C}_-$. $\alpha = \bar{\alpha}_C (\beta)$ is the limiting curve of $\alpha = \alpha_C (\beta, \epsilon)$ as $\epsilon \to 0$ (dotted line).

Numerical computations indicate that the canard line $\alpha = \alpha_C (\beta, \epsilon)$ and the line $\alpha = \bar{\alpha}_C (\beta)$ both intersect the Takens-Bogdanov point (β_T, α_T). Moreover, as $\epsilon \to 0$, $\alpha = \alpha_C (\beta, \epsilon)$ converges to $\alpha = \bar{\alpha}_C (\beta)$.

4.2.2 Bifurcations, attractors and simulated waveforms for $1.5 < \beta < 6$, $\alpha < \alpha'$

Recall that the actual object of interest is the gaze time series $\{g(t) : t \geq 0\}$ of the full model (1)-(6) for initial condition with $v(0) = 0$, $n(0) = g(0)$ and $m(0) = \Delta g$, as this simulates a saccade of Δg degrees from an initial gaze angle of $g(0)$. In this section, the various forms of $g(t)$ that the model can produce will be discussed for the limited parameter range $1.5 < \beta < 6$, $\alpha < \alpha'$, for which biologically realistic time series were previously found. Figure 10 is a plot of the burst system bifurcations and attractors for ϵ small and (β, α) restricted to this region (compare with fig. 8). A range of the gaze time series that can arise for parameters from this region is shown in figure 11. Each of these will now be discussed in terms of the corresponding attractor, and the bifurcation giving rise to the attractor.
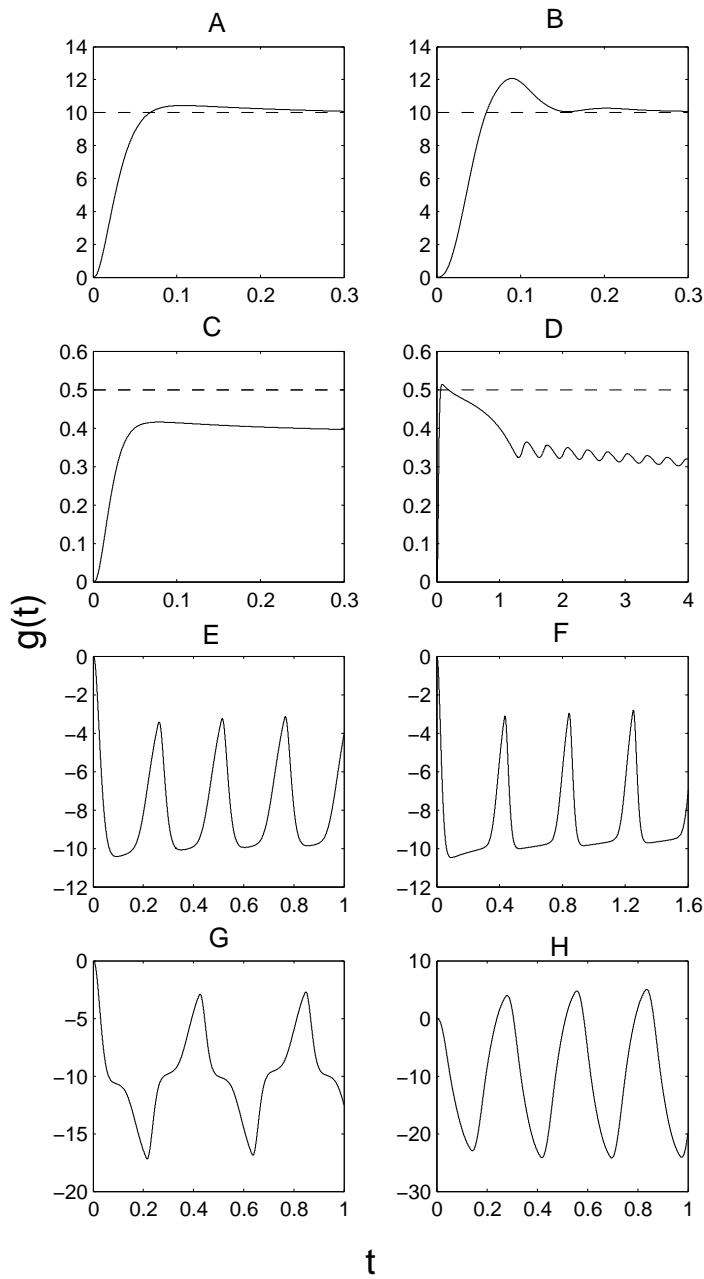
Figure 11: Gaze time series $\{g(t) : t \geq 0\}$ generated by the full model (1)-(6) for initial conditions with $g(0) = v(0) = n(0) = 0$ and $m(0) = \Delta g$. A: $\alpha = 20$, $\beta = 3$, $\epsilon = 0.001$, $\Delta g = 10$. Normometric saccade. B: $\alpha = 20$, $\beta = 3$, $\epsilon = 0.015$, $\Delta g = 10$. Dynamic overshoot. C: $\alpha = 206$, $\beta = 3$, $\epsilon = 0.001$, $\Delta g = 0.5$. Hypometric saccade. D: $\alpha = 207.656$, $\beta = 3$, $\epsilon = 0.006$, $\Delta g = 0.5$. Small-amplitude nystagmus. E: $\alpha = 240$, $\beta = 3$, $\epsilon = 0.004$, $\Delta g = -10$. Jerk CN. F: $\alpha = 240$, $\beta = 3$, $\epsilon = 0.0048$, $\Delta g = -10$. Jerk with extended foveation. G: $\alpha = 240$, $\beta = 3$, $\epsilon = 0.006$, $\Delta g = -10$. Bidirectional jerk CN. H: $\alpha = 240$, $\beta = 3$, $\epsilon = 0.06$, $\Delta g = -10$. Pendular CN.
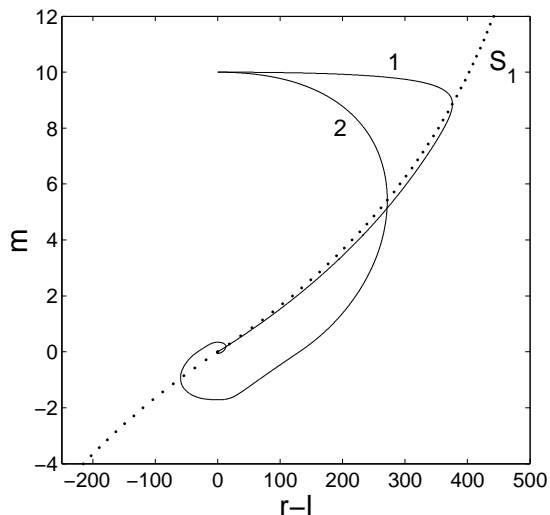
24

Figure 12: Burst system trajectories corresponding to simulated normometric saccades. Trajectory #1: $\alpha = 20$, $\beta = 3$, $\epsilon = 0.001$, $\Delta g = 10$. Trajectory #2: $\alpha = 20$, $\beta = 3$, $\epsilon = 0.015$, $\Delta g = 10$. The dotted line denotes the slow manifold S_M. The stable manifold L_0 is orthogonal to this projection and passes through $(0,0)$. The gaze time series corresponding to trajectories #1 and #2 are shown in figures 11-A and 11-B respectively.

Normometric saccades, hypometric saccades and dynamic overshoots: For $\alpha < \Lambda_+ \beta$ with ϵ small, the origin $\mathbf{0} = (0,0,0)^T$ is the unique attractor of the burst equations. $\mathbf{0}$ is a stable node of $\dot{\mathbf{y}} = \mathbf{G}(\mathbf{y})$ in this range, in the sense that it is a stable node of the smooth systems $\dot{\mathbf{y}} = \mathbf{G}_+(\mathbf{y})$ and $\dot{\mathbf{y}} = \mathbf{G}_-(\mathbf{y})$ introduced in section 4.1.4. For $\alpha < \Lambda_+ \beta$, S_M consists of the single curve S_1. Since ϵ is small, $\mathbf{y}(t)$ contracts rapidly to S_1 parallel to the (r,l) plane, and then converges along S_1 to the origin (see trajectory #1 of figure 12). The corresponding motor error variable $m(t)$ converges quickly to 0. Hence, as suggested by approximation (16), the gaze time series has the form of a normometric (accurate) saccade to $g(0) + \Delta g$ degrees which drifts back to zero like $(g(0) + \Delta g) e^{-\frac{t}{T_N}}$. Figure 11-A shows a simulated normometric saccade (cf. figure 1-A)

Increasing ϵ causes trajectories of $\dot{\mathbf{y}} = \mathbf{G}(\mathbf{y})$ to follow S_1 less closely as they converge to $\mathbf{0}$. Indeed, for $\epsilon > \frac{1}{4\left(\Lambda_+ - \frac{\alpha}{\beta}\right)}$, $D\mathbf{G}_+(\mathbf{0})$ has a pair of complex conjugate eigenvalues $\{\mu, \bar{\mu}\}$ with $Re\{\mu\} < 0$. Trajectories of the smooth systems $\dot{\mathbf{y}} = \mathbf{G}_+(\mathbf{y})$ and $\dot{\mathbf{y}} = \mathbf{G}_-(\mathbf{y})$ spiral around the stable manifold $L_0 = \left\{(x,x,0)^T : x \in \mathbb{R}\right\}$ as they converge to the origin. Since trajectories of the piecewise smooth system $\dot{\mathbf{y}} = \mathbf{G}(\mathbf{y})$ can be constructed by concatenating sections of trajectories of $\dot{\mathbf{y}} = \mathbf{G}_+(\mathbf{y})$ and $\dot{\mathbf{y}} = \mathbf{G}_-(\mathbf{y})$, it follows that $\mathbf{y}(t)$ also spirals around L_0 as it converges to the origin (see trajectory #2 of figure 12). The motor error $m(t)$ converges to 0 by executing damped oscillations about 0. Thus, as suggested by (16), the corresponding gaze time series $g(t)$ has the form of a normometric saccade with a post-saccadic damped oscillation about $(g(0) + \Delta g) e^{-\frac{t}{T_N}}$, which resembles a dynamic

25

overshoot. A numerical example is shown in figure 11-B (cf. figure 1-B).

For $\Lambda_+\beta < \alpha < \alpha_H(\beta)$ with ϵ small, the attractors are the symmetry-related pair of fixed points $\{\mathbf{y}_1^+, \mathbf{y}_1^-\}$, which are stable nodes in this range. As trajectories cannot cross the plane $m = 0$, $\mathbf{y}(t) \to \mathbf{y}_1^+$ as $t \to \infty$ if $\Delta g > 0$ and $\mathbf{y}(t) \to \mathbf{y}_1^-$ as $t \to \infty$ if $\Delta g < 0$. Thus, $m(t) \to sign(\Delta g)\, m_1$ as $t \to \infty$. If $|\Delta g|$ is large compared to m_1, $g(t)$ has the form of a normometric saccade, while if $|\Delta g|$ is of the same order as m_1, $g(t)$ has the form of a hypometric (under-shooting) saccade, as suggested again by approximation (16). Figure 11-C shows a simulated hypometric saccade.

Small-amplitude nystagmus and jerk CN: In the range $\alpha > \alpha_H(\beta)$ with ϵ small, the attractors of the burst equations are the symmetry-related pair of stable limit cycles $\{\mathcal{C}_+, \mathcal{C}_-\}$. Moreover, since trajectories cannot cross the plane $m = 0$, if $\Delta g > 0$, $\mathbf{y}(t)$ converges to $\mathcal{C}_+$, while if $\Delta g < 0$, $\mathbf{y}(t)$ converges to $\mathcal{C}_-$. This situation was discussed in section 3.3 where it was stated that if $m(t)$ converges to a periodic function $m_S(t)$, then $g(t)$ converges to a periodic function $g_S(t)$ which is the result of applying a linear filter to $m_S(t)$ (and consequently has the same period). Indeed, it was argued that if $m_S(t)$ has no significant energy outside the angular frequency range $(0.08, 55)$, then $g_S(t) \approx -m_S(t - t_g) + \langle m_S(t) \rangle$, where $t_g = 0.0115$.

For $\alpha_H(\beta) < \alpha < \alpha_C(\beta, \epsilon)$, $\mathcal{C}_+$ and $\mathcal{C}_-$ are small-amplitude limit cycles. $m_S(t)$, and hence $g_S(t)$, is therefore a small-amplitude periodic oscillation. The corresponding gaze time series $g(t)$ has the form of a normometric saccade with a post-saccadic small-amplitude nystagmus. An example of such a waveform is shown in figure 11-D.

For $\alpha > \alpha_C(\beta, \epsilon)$, $\mathcal{C}_+$ and $\mathcal{C}_-$ are large-amplitude relaxation oscillations. Numerical work suggests that for $\alpha > \bar{\alpha}_C(\beta)$, the intersection of the slow manifold S_M with the plane $m = m'$ has greater extent in the positive $r - l$ direction than in the negative $r - l$ direction, for m' such that there is more than one point of intersection (cf. figures 9-B and 9-C). Since $\dot{m} = -(r - l)$, this configuration of S_M means that for $\alpha > \alpha_C(\beta, \epsilon)$, the contraction of $\mathcal{C}_+$ onto S_M parallel to the (r, l) plane results in $\dot{m}$ changing rapidly from small and positive to large and negative (cf. figure 9-C). (By symmetry, the contraction of $\mathcal{C}_-$ onto S_M results in $\dot{m}$ changing rapidly from small and negative to large and positive). Accordingly, $m_S(t)$ has the form of a slow drift away from $m = 0$ followed by a sudden switch to a faster return towards $m = 0$ that resembles a jerk nystagmus. For $\Delta g > 0$, $m_S(t)$ resembles a left-beating jerk CN and for $\Delta g < 0$, $m_S(t)$ resembles a right-beating jerk CN. The approximation $g_S(t) \approx -m_S(t - t_g) + \langle m_S(t) \rangle$ therefore implies that $g_S(t)$ resembles a jerk nystagmus with a beat direction opposite to that of $m_S(t)$. For a given Δg, the gaze time series $g(t)$ has the form of a normometric saccade with a post-saccadic oscillation which decays to a periodic jerk CN. The periodic oscillation is right-beating for $\Delta g > 0$ and left-beating for $\Delta g < 0$. Figure 11-E is an example of a simulated left-beating jerk CN (cf. figure 1-C).
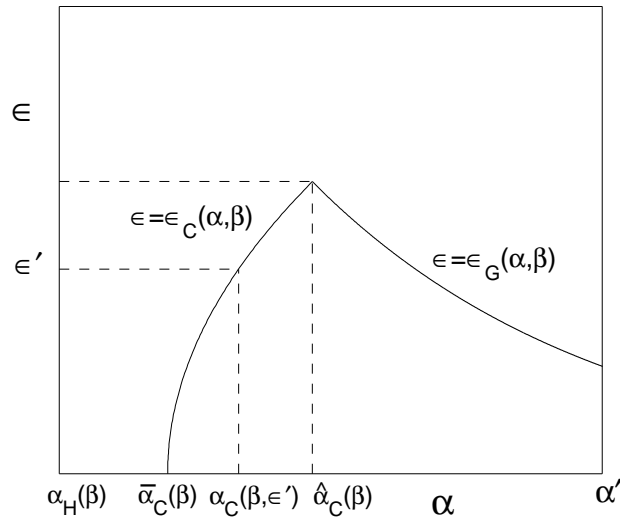
Figure 13: Schematic of the canard surface $\epsilon = \epsilon_C(\alpha, \beta)$ and the gluing-type bifurcation surface $\epsilon = \epsilon_G(\alpha, \beta)$ in the (α, ϵ) plane for a fixed β with $1.5 < \beta < 6$. The curve $\alpha = \hat{\alpha}_C(\beta)$ represents the projection onto the (β, α) plane of the intersection of $\epsilon = \epsilon_C(\alpha, \beta)$ with $\epsilon = \epsilon_G(\alpha, \beta)$.

Jerk with extended foveation, bidirectional jerk and pendular CN: As ϵ is increased in the range $\alpha > \bar{\alpha}_C(\beta)$, the canards describe a surface $\epsilon = \epsilon_C(\alpha, \beta)$ in $(\alpha, \beta, \epsilon)$ space such that: i) the curve $\alpha = \bar{\alpha}_C(\beta)$ is the intersection of $\epsilon = \epsilon_C(\alpha, \beta)$ with the (β, α) plane, and ii) for a given value ϵ' of ϵ, the curve $\alpha = \alpha_C(\beta, \epsilon')$ is the projection onto the (β, α) plane of the intersection of $\epsilon = \epsilon_C(\alpha, \beta)$ with the plane $\epsilon = \epsilon'$. Numerical work suggests that as ϵ is increased in $(\alpha, \beta, \epsilon)$ space, the canard surface terminates by intersecting a surface of gluing-type bifurcations, which will be written $\epsilon = \epsilon_G(\alpha, \beta)$. A schematic of the curves $\epsilon = \epsilon_C(\alpha, \beta)$ and $\epsilon = \epsilon_G(\alpha, \beta)$ in the (α, ϵ) plane for a fixed β is shown in figure 13 to aid their visualisation.

At $\epsilon = \epsilon_G(\alpha, \beta)$, $\mathcal{C}_+$ and $\mathcal{C}_-$ merge, forming a single symmetry-invariant limit cycle written as $\mathcal{C}$. This bifurcation is qualitatively equivalent to a symmetric, smooth gluing bifurcation of the saddlenode type ([26]), and is a result of $\mathcal{C}_+$ and $\mathcal{C}_-$ undergoing simultaneous saddlenode homoclinic bifurcations at the origin in the smooth systems $\dot{\mathbf{y}} = \mathbf{G}_+(\mathbf{y})$ and $\dot{\mathbf{y}} = \mathbf{G}_-(\mathbf{y})$ respectively. Figure 14 shows the gluing of the limit cycles as ϵ increases through $\epsilon = \epsilon_G(\alpha, \beta)$ for $\alpha = 240$ and $\beta = 3$.

Let $\alpha = \hat{\alpha}_C(\beta)$ denote the curve corresponding to the projection onto the (β, α) plane of the intersection of $\epsilon = \epsilon_C(\alpha, \beta)$ with $\epsilon = \epsilon_G(\alpha, \beta)$ (see figure 13). As ϵ is increased from 0 for $\alpha \in (\bar{\alpha}_C(\beta), \hat{\alpha}_C(\beta))$, the large-amplitude limit cycles $\mathcal{C}_+$ and $\mathcal{C}_-$ undergo canards becoming small-amplitude limit cycles. Increasing ϵ from 0 for $\alpha \in (\hat{\alpha}_C(\beta), \alpha')$ causes $\mathcal{C}_+$ and $\mathcal{C}_-$ to undergo the gluing bifurcation. As $\epsilon \to \epsilon_G(\alpha, \beta) -$ in this range, the limit cycles $\mathcal{C}_+$ and $\mathcal{C}_-$ approach homoclinicity, resulting in $m_S(t)$ developing increasingly long periods where it is approximately equal to 0. For $\epsilon < \epsilon_G(\alpha, \beta)$ with $|\epsilon - \epsilon_G(\alpha, \beta)|$ small, $m_S(t)$,
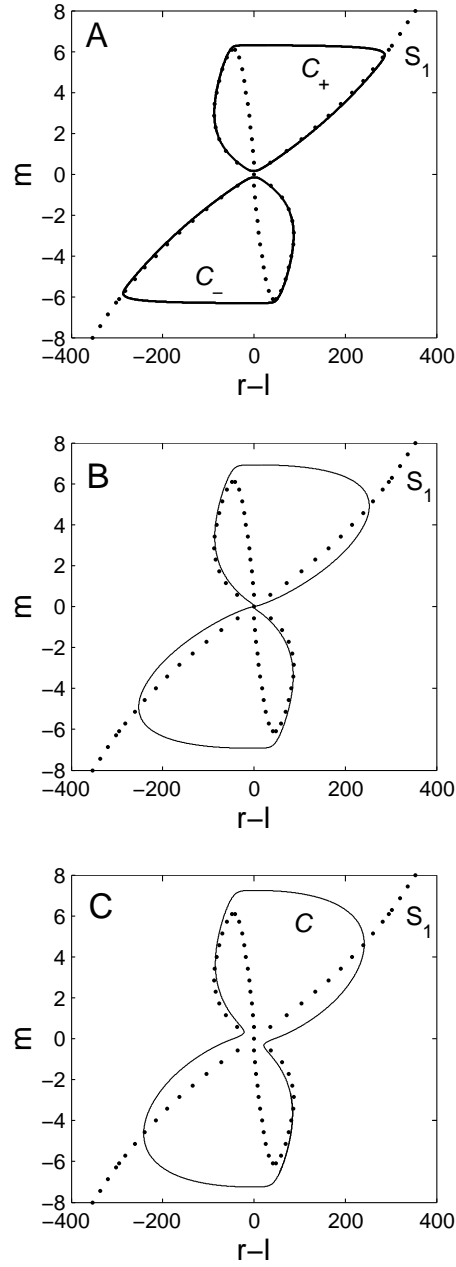
27

Figure 14: Projection into the $(r - l, m)$ plane of the nonsmooth gluing bifurcation which occurs in the burst equations for $\alpha = 240$, $\beta = 3$. A: $\epsilon = 0.0005$. B. $\epsilon = \epsilon_G(\alpha, \beta) \approx 0.00490167$. C. $\epsilon = 0.008$. The dotted lines denote the slow manifold S_M.

28

and hence $g_S(t)$, resembles a jerk nystagmus with an extended foveation period. The gaze time series $g(t)$ has the form of a normometric saccade with a post-saccadic oscillation which decays to a periodic jerk nystagmus with an extended foveation period. Figure 11-F is an example of such a simulated waveform (cf. figure 1-D).

For $\epsilon > \epsilon_G(\alpha, \beta)$, provided that $\epsilon - \epsilon_G(\alpha, \beta)$ is not too large, $\mathcal{C}$ is a relaxation oscillation with portions lying on S_M (see figure 14-C). $m_S(t)$ is composed of slow drifts away from 0 followed by fast returns towards 0 in alternating directions, and resembles a bidirectional jerk nystagmus. The approximation relating $g_S(t)$ and $m_S(t)$ implies that $g_S(t)$ also resembles a bidirectional jerk nystagmus. $g(t)$ has the form of a normometric saccade which decays to a periodic bidirectional jerk oscillation, as can be seen in figure 11-G (cf. figure 1-E). As $\epsilon \to \epsilon_G(\alpha, \beta)+$, $\mathcal{C}$ approaches homoclinicity, and $g_S(t)$ resembles a bidirectional jerk nystagmus with an extended foveation period.

Increasing ϵ from $\epsilon_G(\alpha, \beta)$ causes the limit cycle $\mathcal{C}$ to be successively less confined to the slow manifold, and to lose the form of a relaxation oscillation. $m_S(t)$ loses its slow-fast form, developing increasingly shorter foveation periods. For sufficiently large ϵ, $m_S(t)$ is sinusoidal with no discernible foveation period, and resembles a pendular nystagmus oscillation. $g_S(t)$ inherits this morphology, and $g(t)$ has the form of a hypermetric (over-shooting) saccade which decays to a periodic pendular nystagmus. Figure 11-H is an example of a pendular nystagmus simulated by the model (cf. figure 1-F).

Other global bifurcations are observed numerically as ϵ is increased for (β, α) in the range $1.5 < \beta < 6$, $\alpha < \hat{\alpha}_C(\beta)$, but these do not have any obvious biological interpretation. In $(\alpha, \beta, \epsilon)$ space, one of these bifurcation surfaces appears to intersect the canard surface $\epsilon = \epsilon_C(\alpha, \beta)$ along the line where it intersects the surface of nonsmooth gluing bifurcations $\epsilon = \epsilon_G(\alpha, \beta)$ [10].

The simulated eye movements generated in the parameter ranges discussed above are summarised in figure 15. Numerical work indicates that $\hat{\alpha}_C(\beta) - \alpha_H(\beta)$ is a decreasing function of β on $(1.5, 6)$. Since $m_H < 1.5$, $\alpha_H(\beta)$ is increasing on $(1.5, 6)$, from which it follows that

$$\frac{\hat{\alpha}_C(\beta) - \alpha_H(\beta)}{\alpha_H(\beta)} < \frac{\hat{\alpha}_C(1.5) - \alpha_H(1.5)}{\alpha_H(1.5)}$$

in this range. Evaluating $\alpha_H(1.5)$ and estimating $\hat{\alpha}_C(1.5)$ implies $\frac{\hat{\alpha}_C(1.5) - \alpha_H(1.5)}{\alpha_H(1.5)} < 0.0055$. Hence, $\hat{\alpha}_C(\beta) \approx \alpha_H(\beta)$ on $(1.5, 6)$: the curves $\alpha = \alpha_H(\beta)$ and $\alpha = \hat{\alpha}_C(\beta)$ lie very close to each other in the (β, α) plane.

5 Implications of the model

5.1 CN may be caused by an abnormal saccadic braking signal

The current control systems view is that CN either results from an instability of the oculomotor control subsystem responsible for gaze-holding, or an instability of the system
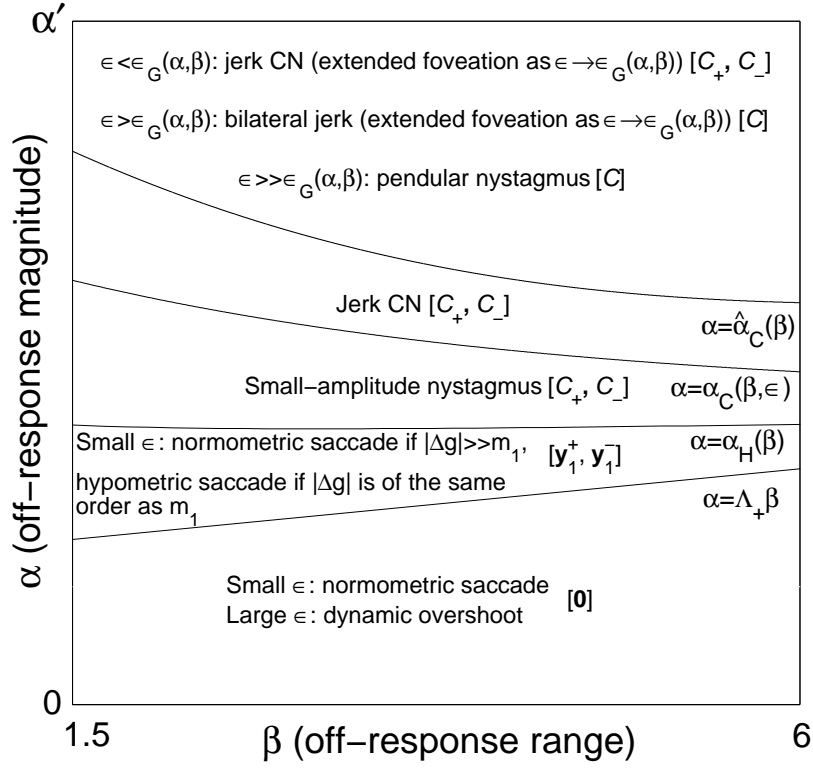
Figure 15: Schematic plot showing the range of eye movements simulated by the saccadic system model (1)-(6). The corresponding attractors of the burst equations (4)-(6) are shown in square brackets. $\alpha = \Lambda_+\beta$ is a line of nonsmooth pitchfork bifurcations at which the origin $\mathbf{0} = (0,0,0)^T$ goes unstable producing a pair of symmetry-related stable fixed points $\{\mathbf{y}_1^+, \mathbf{y}_1^-\}$. $\alpha = \alpha_H(\beta)$ is a line of symmetry-related supercritical Hopf bifurcations at which $\mathbf{y}_1^+$ and $\mathbf{y}_1^-$ go unstable producing a pair of symmetry-related stable limit cycles $\{\mathcal{C}_+, \mathcal{C}_-\}$. $\alpha = \alpha_C(\beta, \epsilon)$ is a line of symmetry-related Hopf-initiated canards at which $\mathcal{C}_+$ and $\mathcal{C}_-$ undergo a sudden increase in amplitude, becoming relaxation oscillations. $\alpha = \hat{\alpha}_C(\beta)$ is the projection onto the (β, α) plane of the intersection of the canard surface $\epsilon = \epsilon_C(\alpha, \beta)$ with the surface of nonsmooth gluing bifurcations $\epsilon = \epsilon_G(\alpha, \beta)$ (see figure 13). As ϵ increases through $\epsilon_G(\alpha, \beta)$ for $\alpha > \hat{\alpha}_C(\beta)$, $\mathcal{C}_+$ and $\mathcal{C}_-$ become homoclinic to the origin and merge, producing a symmetry-invariant limit cycle $\mathcal{C}$. α, β and ϵ represent respectively the off-response magnitude, off-response range and response time of the saccadic burst neurons.

responsible for tracking slowly moving targets (the smooth pursuit system) [33], [30], [21]. The saccadic system is invariably assumed to be functioning normally in the control models, presumably as a consequence of the fact that CN subjects produce predominately accurate saccades [45]. Possibly the most significant implication of the model is that it suggests congenital nystagmus may in fact be a disorder of the saccadic system. Moreover, the analysis implies that jerk CN is one of a range of disorders generated as the burst neuron off-response magnitude α is increased (see figure 15).

Recalling that the off-response corresponds to a braking signal gives a physiological interpretation of the modelled dysmetrias and oscillations. Hypometric saccades can be attributed to a braking signal which has increased in strength to a level where it is causing the eye to be brought to a halt before the target gaze angle is achieved. The oscillatory disorders simulated by the model may be thought of as resulting from a braking signal of sufficient strength to produce a significant movement of the eye in the opposite direction to that of the saccade. This reverse motion in turn causes the onset of an oscillatory instability through the mutual inhibition of the burst neurons.

The suggestion that CN is due to an abnormal braking signal is difficult to test since it requires a normal braking signal/off-response to be accurately defined. Nonetheless, the fact that a model of the fast eye movement system alone can generate both the slow and fast phases of CN does indicate that the ability of CN subjects to generate normal saccades is not sufficient basis to conclude that the instability must be a slow eye movement disorder.

5.2   The fast phases of CN may not be corrective

The model analysis implies that the slow-fast form of jerk and bidirectional jerk oscillations may be a consequence of the geometry of an underlying slow manifold in the saccadic phase space. This contrasts with the control models which assume that the fast phases of the oscillations are corrective saccades that return the eye to the target following drift due to a slow eye movement instability [33], [30], [21].

The alternative view proposed here is consistent with the finding that the peak velocities of CN fast phases follows a saccadic main sequence distribution [9]. The segment of the slow manifold along which trajectories that simulate normometric saccades contract to the origin corresponds to the initial rapid movement of the eye towards the target gaze angle (see trajectory #1 of figure 12). Consequently, the form of this segment determines the relationship between the peak velocities and amplitudes of saccades that defines the main sequence. As can be seen in figures 14-A and 14-C, the portions of the limit cycles $\mathcal{C}_+$, $\mathcal{C}_-$ and $\mathcal{C}$ which correspond to the fast phases of the corresponding simulated jerk and bidirectional jerk oscillations all lie along this same segment: the fast phases therefore follow the saccadic main sequence.

5.3 The most likely pathological oscillation is a jerk, bidirectional jerk or pendular nystagmus

The analysis of the model implies that if the system is in the oscillatory regime $\alpha > \alpha_H(\beta)$, the oscillation is likely to be a jerk, bidirectional jerk or pendular nystagmus. This follows from the fact that $\hat{\alpha}_C(\beta) \approx \alpha_H(\beta)$ on $(1.5, 6)$, as discussed at the end of section 4.2.2. Hence, as a result of the existence of the canard, only a small increase in the braking signal strength α is required to push the system into the range $\alpha > \hat{\alpha}_C(\beta)$ in which the possible waveform types are those mentioned above. The intermediate small-amplitude oscillation is unlikely to be observed (see figure 15).

This prediction is consistent with the findings of a recent major clinical eye movement study [2]. Of the 161 CN subjects with a dominant waveform type used in the study, all had oscillations with amplitude greater than 0.3 degrees: no subjects with sustained small-amplitude oscillations were reported. Moreover, 73% of the subjects exhibited jerk, bidirectional jerk, or pendular nystagmus oscillations, while 22% had oscillations which were variations on these basic waveforms, such as pseudocycloid or pendular with foveating saccades.

5.4 Dynamic overshoot is caused by reversals of the saccadic control signal

It was argued in section 4.2.2 that increasing the burst neuron response time ϵ causes burst system trajectories to follow the slow manifold S_M less closely as they converge to the origin. This results in oscillations of both the motor error signal m and the saccadic control signal $b = r - l$ as they converge to 0 (see figure 12). These oscillations are converted by the muscle plant into a gaze signal g which oscillates about the desired gaze angle $g(0) + \Delta g$, and thus simulates a dynamic overshoot (see figure 11-B).

The ability of the model to generate dynamic overshoots in the range $\alpha < \Lambda_+ \beta$ is consistent with the observation that normal subjects can exhibit dynamic overshoots in addition to normometric saccades. Moreover, the suggestion that the overshoots are attributable to oscillations of the saccadic control signal agrees with the predictions of a psychophysical study of dynamic overshoots carried out by Bahill et al [12]. Bahill et al proposed that the characterisation of the muscle plant as an overdamped harmonic oscillator implies that the reversals in eye direction observed during dynamic overshoot are likely to be caused by reversals of the saccadic control signal. Furthermore, they suggested that a possible physiological cause of the reversals was post-inhibitory rebound firing of the burst neurons, possibly accentuated by movements of the centre of rotation of the eye during saccades [12].

The work presented here provides a simpler explanation for the reversals, namely the spiralling of trajectories around the origin in the burst neuron firing rate versus motor

error phase plane, resulting from an increased burst neuron response time. The spiralling of trajectories is independent of the inhibition between the right and left burst neurons, and can be reproduced by a simplified model which does not incorporate mutual inhibition terms in the equations for the burst neurons [7].

5.5 The evolution from jerk CN to bidirectional jerk CN is caused by a gluing bifurcation

If ϵ is increased in the (β, α) range $1.5 < \beta < 6$, $\alpha > \hat{\alpha}_C(\beta)$, the model simulates the transition from jerk nystagmus to bidirectional jerk and then pendular nystagmus observed in some subjects as the initial gaze angle $g(0)$ is varied, or their level of attention is reduced [4], [5]. As ϵ corresponds to the speed at which the burst neurons respond to the motor error signal m, an increase in ϵ might be interpreted as a decrease in the attention level of the subject, and so the modelled waveform evolution is consistent with that observed experimentally when the attention level is reduced. The evolution from jerk to bidirectional jerk that is seen in some subjects as the gaze angle passes close to the neutral zone ([8]) cannot, however, be accounted for by the model in its current form, since $g(0)$ is not a parameter of the model. Additionally, the beat direction of the simulated jerk waveforms is dependent on the required gaze displacement Δg instead of $g(0)$. These observations suggest incorporating $g(0)$ explicitly in the equations. The analysis of the basic model presented here would provide the platform for a quantitative assessment of the effect of such a modification.

Despite these limitations, the model does propose a specific underlying mechanism for the jerk to bidirectional jerk transition, namely the merging of a pair of limit cycle attractors in a gluing bifurcation. This is a novel explanation for the qualitative change in the underlying neurobiological oscillator which could form the basis of a new technique to control CN oscillations. A recent experimental study demonstrated that a transient change from a unidirectional to a bidirectional jerk waveform could be induced in a CN subject by forcing the target with a periodic waveform [19]. The waveform used in this study was an unstable periodic orbit extracted from a previous recording of the subject's eye movements using the technique of So et al [38]. The gluing bifurcation mechanism suggested here implies the possibility of establishing more sophisticated control over the jerk waveform by using periodic forcing so as to bring the system close to homoclinicity. Such a technique could have clinical applications, as the increased foveation times should lead to the development of improved visual resolution.

References

[1] Abadi, R.V.: Mechanisms underlying nystagmus. J. R. Soc. Med. **95**, 1–4 (2002)

[2] Abadi, R.V., Bjerre, A.: Motor and sensory characterisitics of infantile nystagmus. Br. J. Ophthalmol. **86**, 1152–1160 (2002)

[3] Abadi, R.V., Broomhead, D.S., Clement, R.A., Whittle, J.P., Worfolk, R.: Dynamical systems analysis: A new method of analysing congenital nystagmus waveforms. Exp. Brain Res. **117**, 355–361 (1997)

[4] Abadi, R.V., Dickinson, C.M.: Waveform characteristics in congenital nystagmus. Doc. Ophthalmol. **64**, 153–167 (1986)

[5] Abadi, R.V., Dickinson, C.M., Pascal, E., Whittle, J., Worfolk, R.: Sensory and motor aspects of congenital nystagmus. In: Schmid, R., Zambarbieri, D. (eds.) Oculomotor Control and Cognitive Processes, pp. 249–262. Elsevier Science Publishers B. V. (North-Holland) (1991)

[6] Abadi, R.V., Sandikcioglu, M.: Visual resolution in congenital pendular nystagmus. Am. J. Optom. Phys. Opt. **52**, 573–581 (1975)

[7] Abadi, R.V., Scallan, C.J., Clement, R.A.: The characteristics of dynamic overshoots in square-wave-jerks and in congenital and manifest latent nystagmus. Vision Res. **40**, 2813–2829 (2000)

[8] Abadi, R.V., Whittle, J.: The nature of head postures in congenital nystagmus. Arch. Ophthalmol. **109**, 216–220 (1991)

[9] Abadi, R.V., Worfolk, R.: Retinal slip velocities in congenital nystagmus. Vision Res. **29**(2), 195–205 (1989)

[10] Akman, O.E.: Analysis of a nonlinear dynamics model of the saccadic system. Ph.D. thesis, Department of Mathematics, University of Manchester Institute of Science and Technology (2003)

[11] Arrowsmith, D.K., Place, C.M.: An Introduction to Dynamical Systems. CUP (1990)

[12] Bahill, A.T., Clark, M.R., Stark, L.: Dynamic overshoot in saccadic eye movements is caused by neurological control signal reversals. Exp. Neurol. **38**, 107–122 (1975)

[13] Bahill, A.T., Clark, M.R., Stark, L.: The main sequence, a tool for studying human eye movements. Math. Biosci. **24**, 191–204 (1975)

[14] Becker, W., Jurgens, R.: An analysis of the saccadic system by means of double step stimuli. Vision Res. **19**, 967–983 (1979)

[15] Becker, W., Klein, H.M.: Accuracy of saccadic eye movements and maintenance of eccentric eye positions in the dark. Vision Res. **13**, 1021–1034 (1973)

[16] Bedell, H.E., Loshin, D.S.: Interrelations between measures of visul acuity and parameters of eye movement in congenital nystagmus. Invest. Ophth. Vis. Sci. **32**, 416–421 (1991)

[17] Boghen, D., Troost, B.T., Daroff, R.B., Dell'Osso, L.F., Birkett, J.E.: Velocity characteristics of human saccades. Invest. Ophth. Vis. Sci. **13**(8), 619–623 (1974)

[18] Broomhead, D.S., Clement, R.A., Muldoon, M.R., Whittle, J.P., Scallan, C., Abadi, R.V.: Modelling of congenital nystagmus waveforms produced by saccadic system abnormalities. Biol. Cybern. **82**, 391–399 (2000)

[19] Clement, R.A., Abadi, R.V., Broomhead, D.S., Whittle, J.P.: Periodic forcing of congenital nystagmus. In: Boccaletti, S., Gluckman, B.J., Kurths, J., Pecora, L.M., Spano M.L. (eds.) Experimental Chaos (Proceedings of the 6th Experimental Chaos Conference, Potsdam, Germany, 2001). AIP (2002)

[20] Clement, R.A., Whittle, J.P., Muldoon, M.R., Abadi, R.V., Broomhead, D.S., Akman, O.: Characterisation of congenital nystagmus waveforms in terms of periodic orbits. Vision Res. **42**, 2123–2130 (2002)

[21] Dell'Osso, L.F.: Nystagmus basics: Normal models that simulate dysfunction. In: Hung, G.K., Ciuffreda, K.J. (eds.) Models of the Visual System, pp. 711–739. Kluwer Academic (2002)

[22] Dell'Osso, L.F., Daroff, M.D.: Congenital nystagmus waveforms and foveation strategy. Doc. Ophthalmol. **39**, 155–182 (1975)

[23] Ditchburn, R.W.: Eye Movements and Visual Perception. Clarendon Press, Oxford (1973)

[24] Enderle, J.D.: Neural control of saccades. In: Hyona, J., Munoz, D.P., Heide, W., Radach, R. (eds.) The Brain's Eye: Neurobiological and Clinical Aspects of Oculomotor Research, vol. 140, pp. 21–49. Elsevier, Amsterdam (2002)

[25] Gancarz, G., Grossberg, G.: A neural model of the saccade generator in the reticular formation. Neural Networks **11**, 1159–1174 (1998)

[26] Glendinning, P.: Global bifurcations in flows. In: Bedford, T., Swift, J. (eds.) New Directions in Dynamical Systems, pp. 120–149. CUP (1988)

[27] Golubitsky, M.: Singularities and Groups in Bifurcation Theory. Springer Verlag (1985)

[28] Guckenheimer, J., Hoffman, K., Weckesser, W.: Numerical computation of canards. Int. J. Bifurcat. Chaos **10**(12), 2669–2687 (2000)

[29] Guckenheimer, J., Holmes, P.: Nonlinear Oscillations, Dynamical Systems and Bifurcations of Vector Fields. Springer Verlag (1983)

[30] Harris, C.M.: Problems in modelling congenital nystagmus: Towards a new model. In: Findlay, J.M., Walker, R., Kentridge, R.W. (eds.) Eye Movement Research: Mechanisms, Processes and Applications, pp. 239–253. Elsevier, Amsterdam (1995)

[31] Hirsch, M.W., Smale, S.: Differential Equations, Dynamical Systems and Linear Algebra. Academic Press (1974)

[32] Kreyszig, E.: Advanced Engineering Mathematics, 7th edn. John Wiley (1993)

[33] Optican, L.M., Zee, D.S.: A hypothetical explanation of congenital nystagmus. Biol. Cybern. **50**, 119–134 (1984)

[34] Robinson, D.A.: The mechanics of human saccadic eye movements. J. Physiol. **174**, 245–264 (1964)

[35] Robinson, D.A.: Models of the saccadic eye movement control system. Kybernetik **14**, 71–83 (1973)

[36] Scudder, C.A.: A new local feedback model of the saccadic burst generator. J. Neurophysiol. **59**, 1455–1475 (1988)

[37] Shelhamer, M.: On the correlation dimension of optokinetic nystagmus eye movements: Computational parameters, filtering, nonstationarity and surrogate data. Biol. Cybern. **76**, 237–250 (1997)

[38] So, P., Ott, E., Sauer, T., Gluckman, B.J., Grebogi, C., Schiff, S.: Extracting unstable periodic orbits from chaotic time series data. Phys. Rev. E **55**, 5398–5417 (1997)

[39] Sparks, D.L.: The brainstem control of saccadic eye movements. Nature Rev. Neurosci. **3**, 952–964 (2002)

[40] Stark, J.: Invariant graphs for forced systems. Physica D **109**, 163–179 (1997)

[41] Tusa, R.J., Zee, D.S., Hain, T.C., Simonsz, H.J.: Voluntary control of congenital nystagmus. Clin. Vision Sci. **7**, 195–210 (1992)

[42] Van Gisbergen, J.A.M., Robinson, D.A., Gielen, S.: A quantitative analysis of generation of saccadic eye movements by burst neurons. J. Neurophysiol. **45**, 417–442 (1981)

[43] Westheimer, G.: Mechanism of saccadic eye movements. Arch. Ophthalmol. **52**, 710–724 (1954)

[44] Westheimer, G., McKee, S.P.: Visual acuity in the presence of retinal image motion. J. Opt. Soc. Am. **65**, 847–850 (1975)

[45] Worfolk, R., Abadi, R.V.: Quick phase programming and saccadic re-orientation in congenital nystagmus. Vision Res. **31**(10), 1819–1830 (1991)

[46] Zeeman, E.C.: Differential equations for the heartbeat and nerve impulse. In: Waddington, C.H. (ed.) Towards a Theoretical Biology, pp. 8–67. University Press, Edinburgh (1972)